Follicular lymphoma triggers phenotypic and functional remodeling of the human lymphoid stromal cell landscape

Frédéric Mourcin, Léa Verdière, David Roulois, Rada Amin, Claire Lamaison, Vonick Sibut, Brice Thamphya, Céline Pangault, Céline Monvoisin, Sarah Huet, et al.

Follicular lymphoma triggers phenotypic and functional remodeling of the human lymphoid stromal cell landscape

Frédéric Mourcin[1], Léa Verdière[1*], David Roulois[1*], Rada Amin[1], Claire Lamaison[1], Vonick Sibut[1], Brice Thamphya[1], Céline Pangault[1,2], Céline Monvoisin[1], Sarah Huet[3,4], Marine Seffals[5], Sylvain Baulande[6], Fatima Mechta-Grigoriou[7], Patricia Legoix[6], Delphine Rossille[1,2], Marion Guirriec[1], Simon Léonard[1], Guillaume Cartron[8], Gilles Salles[9], Thierry Fest[1,2] and Karin Tarte[1,2,10,*]

[1] UMR 1236, Univ Rennes, INSERM, Etablissement Français du Sang Bretagne, F-35043, Rennes, France

[2] Pôle Biologie, CHU Rennes, F-35033 Rennes, France

[3] Université Claude Bernard Lyon I, Equipe Lymphoma Immuno Biology, Equipe Labellisée par la Ligue Nationale contre le Cancer, F-69921 Oullins, France

[4] Hospices Civils de Lyon, Service d'hématologie biologique, F-69395 Pierre-Bénite, France

[5] UMS Biosit, Core Facility H2P2, Univ Rennes, INSERM, CNRS, Rennes, F-35043, France

[6] Institut Curie Genomics of Excellence (ICGex) Platform, Institut Curie Research Center, PSL Research University, F-75005, Paris, France

[7] Institut Curie, Stress and Cancer Laboratory, Equipe Labellisée par la Ligue Nationale contre le Cancer, PSL Research University, 26, rue d'Ulm, F-75248 Paris, France

[8] Department of Hematology, CHU Montpellier, F-34000, Montpellier, France

[9] Lymphoma Service, Memorial Sloan Kettering Cancer Center , NY, USA

[10] Lead contact

* Correspondence: karin.tarte@univ-rennes1.fr

RA Current address:

Department of Biochemistry, Beadle center, University of Nebraska at Lincoln, NE, 68503, USA

* these authors contributed equally to this work

SUMMARY

Lymphoid stromal cells (LSCs) are essential organizers of immune responses. We analyzed tonsillar tissue by combining flow cytometry, *in situ* imaging, RNA-sequencing, and functional assays, thus defining three distinct human LSC subsets. The integrin CD49a designated perivascular stromal cells exhibiting features of local committed LSC precursors. CD49a also segregated cytokine/chemokine-producing fibroblastic reticular cells (FRCs) supporting naive B cell and T cell survival. The follicular dendritic cell (FDC) transcriptional profile reflected active responses to B cell and non-B cell stimuli. We therefore examined the impact of B cell stimuli on LSCs in follicular lymphoma (FL). FL B cells interacted primarily with CD49a$^+$ FRCs. Transcriptional analyses revealed LSC reprogramming *in situ* downstream of the cytokines tumor necrosis factor (TNF) and transforming growth factor β (TGF-β), including increased expression of the chemokines CCL19 and CCL21. Our findings define human LSC populations in healthy tissue and reveal bidirectional crosstalk between LSCs and malignant B cells that may present a targetable axis in lymphoma.

INTRODUCTION

Secondary lymphoid organs (SLOs) are immunological meeting places where antigen-dependent adaptive immunity is controlled through finely regulated interactions between immune cells, endothelial cells, and specialized fibroblastic cells of mesenchymal origin called lymphoid stromal cells (LSCs) (Mueller and Germain, 2009). LSCs are essential coordinators of the functionally distinct microenvironmental niches that support lymphocyte recruitment, survival, activation, and differentiation (Krishnamurty and Turley, 2020). Expression of gp38/Podoplanin (Pdpn) and lack of the endothelial marker CD31 define mouse mature LSCs within the nonhematopoietic compartment, as opposed to Pdpn$^-$CD31$^-$ LSCs (Malhotra et al., 2012). However, Pdpn$^+$ LSCs encompass different cell subsets. CD21$^+$ follicular dendritic cells (FDCs), populating the center of B cell follicles, regulate selection of antigen-specific B cells. CD21$^-$ fibroblastic reticular cells (FRCs), residing outside follicles, support antigen delivery, naive lymphocyte and mature dendritic cell recruitment, and T cell survival and activation (Perez-Shibayama et al., 2019). Similarly, the Pdpn$^-$CD31$^-$ LSC population is heterogeneous, including myofibroblastic progenitors of the perivascular space that are proposed to be adult LSC progenitors (Chai et al., 2013; Cheng et al.,

2019; Krautler et al., 2012). LSC diversity is only partially resolved (Rodda et al., 2018; Takeuchi et al., 2018). In particular, specific FRC subsets support naive B cell survival in the T cell zone (Cremasco et al., 2014), contribute to plasmablast exit from the germinal center (GC) (Zhang et al., 2018), or support plasma cell survival in the medulla (Huang et al., 2018), thus increasing the diversity of LSC subsets contributing to B cell fate. In this rapidly evolving field, human LSCs remain poorly defined at both transcriptomic and functional levels. Studies on human FRCs utilize long-term *in vitro* expanded cells, introducing potential culture-related artifacts (Bar-Ephraim et al., 2016; Knoblich et al., 2018; Severino et al., 2017). Moreover, the lack of data on native FDCs and $PDPN^{-}CD31^{-}$ LSCs preclude any conclusion on human LSC heterogeneity, origin, and pathogenic role.

Besides cell-intrinsic heterogeneity, LSCs possess dynamic plasticity in response to extrinsic stimuli. Once an adaptive immune response is initiated, FRCs proliferate and relax their actomyosin cytoskeleton, thus accommodating the rapid increase of lymphocyte number (Astarita et al., 2015; C.-Y. Yang et al., 2014). Such physiological responses could be hampered in many pathological settings, including chronic infections, autoimmunity, and cancers (Fletcher et al., 2015). In particular, FRCs within tumor-draining lymph nodes (LNs) can undergo structural remodeling and transcriptional modifications reminiscent to that of cancer-associated fibroblasts (CAFs). Such stroma reprogramming then impacts local immune-cell composition and promotes an immunosuppressive tumor-supportive niche (Riedel et al., 2016).

In follicular lymphoma (FL), the most frequent indolent lymphoma, malignant B cells are strongly dependent on a permissive lymphoid microenvironment including follicular helper T cells (Tfh), and LSCs (Amé-Thomas and Tarte, 2014; Huet et al., 2018a; Lamaison and Tarte, 2019). FL is thus one of the best paradigms of LSC-related cancer. Whereas FL B cells exhibit the general hallmark of GC centrocytes, FL LNs are characterized by a disappearance of $CD21^{+}$ FDCs and an amplification of LSCs overexpressing CXCL12 and the FRC marker transglutaminase (Pandey et al., 2017). However, FL-infiltrating LSC heterogeneity and origin are largely unexplored. *In vitro* expanded FL stromal cells exhibit specific phenotypic, transcriptomic, and functional features associated with direct tumor B cell supportive functions. FL stromal cells also display an increased capacity to recruit and activate other components of the tumor cell niche (Grégoire et al., 2015; Guilloton et al., 2012). FL B cells likely participate in the activation of LSC meshwork within malignant LNs as highlighted by their capacity

to trigger *in vitro* the commitment of mesenchymal precursors into FRC-like cells able in turn to support their survival (Amé-Thomas et al., 2007). How native human FRCs could promote FL tumor cell survival and how FL-infiltrating LSCs display tumor-induced modifications *in situ* remain unknown.

Here, we characterized sorted human LSC subsets by a combination of phenotypic, transcriptomic, and functional approaches. The integrin α1 subunit, CD49a, identified a subset of clonogenic PDPN$^-$ cells with a perivascular localization and endowed with a LSC precursor phenotype. CD49a also highlighted immunologically competent FRCs able to support naive T and B cell survival. We then revealed that FL B cells primarily interact with human CD49a$^+$ FRCs. Moreover, native FL-infiltrating LSC subsets displayed specific alterations of their gene expression profiles (GEP), validated *in situ* in a large series of FL patients, and consistent with an enhanced capacity to interact with malignant B cells, that in turn contribute to their early reprogramming. Altogether, these data identify FL-LSCs as interesting therapeutic targets.

RESULTS

The integrin CD49a identifies discrete subsets of human LSCs

To comprehensively study human LSCs, we used an enzymatic digestion protocol to reproducibly identify viable stromal cell subsets from tonsils, including CD31$^+$ PDPN$^-$ blood endothelial cells (BEC), CD31$^+$ PDPN$^+$ lymphatic endothelial cells (LEC), and CD31$^-$ LSCs (Figure 1A). Human CD31$^-$ LSCs were further divided into 3 main subsets that expressed increasing amounts of the adhesion molecules VCAM1 and ICAM1: PDPN$^-$CD21$^-$ cells (double negative (DN) LSCs), PDPN$^+$CD21$^-$ cells (PDPN LSCs), and PDPN$^+$CD21$^+$ cells (CD21 LSCs). Histological analyses confirmed *in situ* the PDPN^{hi}VCAM1^{hi}ICAM1^{hi} phenotype of follicular CD21$^+$ LSCs. In comparison, VCAM1 and ICAM expression was reduced on extrafollicular PDPN^{int}CD21$^-$ LSCs (Figure S1A-C). Human PDPN LSCs specifically expressed transglutaminase (TGM2), a marker of extrafollicular LSCs *in situ* (Thomazy et al., 2003), whereas DN LSCs were negative for *PDPN*, *CR2* (encoding CD21), and *TGM2* (Figure S1B-D).

Evaluation of previously described LSC markers revealed that, whereas CD21 LSCs were homogeneously ICAM1^{hi}VCAM1^{hi}PDGFRα$^-$PDGFRβ$^+$CD146$^+$, both PDPN LSCs and DN LSCs displayed varied expression of these markers, suggesting additional levels of heterogeneity (Figure 1B). To investigate the distinctive features of human

LSC subsets, we tested several classical markers of human mesenchymal stem/stromal cells (MSCs) including CD73, CD271, and integrin α1 subunit (CD49a) (data not shown). Flow cytometry analyses identified CD49a as the most discriminant marker of discrete subsets of both DN LSCs and PDPN LSCs, whereas follicular CD21 LSCs were CD49a^{-} (Figure 1C-D and S1E). First, CD49a identified a subset of DN LSCs expressing high levels of CD146 and PDGFRβ in the absence of PDGFRα. Initial depletion of CD45^{+} cells revealed that PDPN^{-}CD49a^{-} DN cells mostly corresponded to residual hematopoietic cells and they were not further studied (Figure S1F). Second, CD49a^{+} PDPN LSCs, unlike CD49a^{-} PDPN LSCs, were homogeneously PDGFRα^{+} and PDGFRβ^{+}, similarly to mouse FRCs (Malhotra et al., 2012). These data support CD49a as a marker segregating phenotypically homogeneous human DN and FRC subsets.

Human LSCs can be divided into 3 subsets with GEP suggesting unique functionality

To evaluate the relationship between LSC phenotype and function, we sorted human LSC subsets and performed single-cell QPCR for a panel of 80 genes known to be associated with stromal cell origin and function. Gene expression segregated CD49a^{+} DN LSCs, CD21 LSC, CD49a^{+}PDPN LSC, and CD49a^{-}PDPN LSCs onto a t-distributed stochastic neighboring embedding (tSNE) plot (Figure 2A). At the single-cell level, 72 genes were differentially expressed between the 4 cell populations ($P < .01$, ANOVA) including 34 classical LSC markers (Figure 2B and S2A). CD49a^{+} DN LSCs expressed genes associated with pericytic identity, like *ABCC9, NOTCH3, MCAM, ITGA7, CSPG4,* together with *ACTA2,* encoding the α-SMA vascular smooth muscle contractility marker, suggesting that they may correspond to the DN LSC subset initially described in mice (Malhotra et al., 2012). The CD21 LSC cluster largely expressed *CR1, CXCL13,* the Fcα/μ receptor *FCAMR,* playing an important role in humoral immune responses (Shibuya and Honda, 2015), and the costimulatory molecule *TNFRSF9,* regulating the GC B cell response (Middendorp et al., 2009), in the absence of *COL4A1, COL1A1,* and *CCL19*. Concerning PDPN LSCs, expression of CD49a identified a cluster enriched for FRC markers including *CCL19, CCL21, CXCL12, COL1A1*, and *COL4A1*. Human CD49a^{+}PDPN LSCs strongly expressed *TNFSF13B*, encoding the B cell survival factor BAFF. CD49a^{-}PDPN LSCs did not express FDC or FRC-related cytokines and chemokines, were thus considered as non-

immunologically competent LSCs, and were not further characterized. Collectively, these data support the identification of three phenotypically distinct subsets of human functional LSCs: CD21 LSCs corresponding to FDCs, CD49a^{+}PDPN LSCs corresponding to FRCs, and CD49a^{+}DN LSCs hereafter called DN cells.

To better investigate the molecular makeup of these 3 human LSC populations, we examined the GEP of sorted FDCs (n=4), FRCs (n=5), and DNs (n=4) by RNA-seq. Principal Component Analysis (PCA) and Pearson correlation analysis adequately segregated the 3 cell subsets (Figure 2C-D). We next explored FDCs, FRCs, and DNs for their expression of cytokines, growth factors, adhesion molecules, extracellular matrix (ECM) components, and immunologically relevant receptors. The differential expression of key immune response regulators depicted the molecular landscape of human LSC functional features (Figure S3). The comparison of our human data to the reference mouse data set (Malhotra et al., 2012) using GSEA approach highlighted the enrichment for mouse DN signature in human DN cells. Conversely, human FRC and FDC profiles were both enriched for the signature of mouse Pdpn^{+} mature LSCs (Figure S2B). We next assessed the 3536 differentially expressed genes between the 3 LSC subsets (Table S1). DN LSCs expressed some genes usually attributed to mature FRCs (685 genes, including *CCL19, CCL21*, and *IL6*) or FDCs (49 genes, including *MFGE8*), raising the hypothesis that human DN LSCs behave as local precursors of FRCs and FDCs (Figure 2E).

To further characterize the molecular pathways that underline the relationship and specificities between human DNs, FRCs, and FDCs, we applied an unsupervised weighted gene co-expression network analysis (WGCNA) to generate transcriptional modules of co-expressed genes and evaluate their relationship to LSC subsets (Figure 2F and S2C). Three modules were significantly associated with a specific LSC subset with an eigengenes value, summarizing the gene expression profile of these modules, above 0.3: DN module (MEblue, 1986 genes, P= .0028), FDC module (MEyellow, 3354 genes, P= .0028), and FRC module (MEpink, 1364 genes, P= .0016) (Figure 2F). We analyzed using Ingenuity Pathway Analysis the genes overexpressed in each LSC-specific module (Figure 2G). The DN module revealed enrichment for genes related to stromal supportive niche functions and the FRC module for genes associated with inflammation and fibrosis. The FDC module highlighted a strong enrichment for metabolic pathways related to the mevalonate metabolism. Collectively, our findings

provide a comprehensive molecular characterization of human LSC populations allowing further functional studies in normal and malignant settings.

The DN LSC subset contains putative human lymphoid stromal precursors

Given the molecular traits of DNs, we assessed their *in situ* localization and identified cells co-expressing α-SMA, CD146, and CD49a in direct contact with the $CD31^+$ endothelium of extrafollicular vessels (Figure 3A). Pericytes and vascular smooth muscle cells, collectively referred to as perivascular cells, are heterogeneous cell subsets playing critical roles in vascular development and homeostasis, and expressing features of mesenchymal progenitors (Armulik et al., 2011). DNs shared with human bone marrow MSCs (BM-MSCs) the expression of CD49a, CD146, and PDGFRβ, in the absence of PDGFRα (Gindraux et al., 2007; Li et al., 2014; Sacchetti et al., 2007). We thus tested *in vitro* the proliferation and differentiation capacities of DNs, looking for potential MSC-like properties. The clonogenic potential of sorted DNs, reflected by the number of colony forming unit-fibroblastic (CFU-F) after 3 weeks of culture, was strongly increased under low oxygen pressure, a common feature with BM-MSCs (Bahsoun et al., 2018) (Figure 3B). Moreover, DNs were able to differentiate into adipocytes, as evaluated by lipid droplet formation, and osteoblasts, as revealed by mineralized matrix deposition, under appropriate culture conditions. In agreement, DNs overexpressed the *NES* progenitor marker, as well as osteoblastic (*DLX5, DLX6*) and pre-adipocytic (*CD36*) markers compared to FRCs and FDCs (Figure 3C). Altogether, these data characterized human DNs as perivascular cells with MSC-like precursor properties and expressing the FRC markers *CCL19* and *CCL21* as well as the FDC-progenitor marker *MFGE8*.

To better characterize the putative phylogenic relationship between DNs and mature LSCs, we then compared the GEP of DNs, FRCs, and FDCs with that of purified BM-MSCs (n=4), representing the standard human stromal cell precursors. The 4 cell subsets could be distinguished in an unsupervised PCA (Figure 3D) and evaluation of the Euclidean distance between them revealed that DNs were significantly closer to mature LSCs than BM-MSCs (Figure 3E). Moreover, the PCA1 axis, that organized a continuum from BM-MSCs, to DNs, FRCs, and ultimately FDCs (Figure 3F), reflected a significant enrichment for genes induced in human stromal cells by tumor necrosis factor alpha (TNF) and lymphotoxin α1β2 (LT) (Dumontet et al., 2021), the two non-

redundant factors triggering LSC differentiation and maintenance (Figure 3G). In agreement, the genes triggering the PCA1 axis were enriched for transcription factor targets of the NF-κB pathway, the main molecular driver of LSC commitment (Figure 3H). *CCL19, CCL21*, and *MFGE8* belonged to the 1671 genes overexpressed in DNs compared to BM-MSCs (Table S2) whereas *CXCL13, TGM2,* and *PDPN* were not expressed by the two cell subsets (Figure 3I) thus confirming that local mesenchymal precursors harbor tissue-specific transcriptomic and functional features (Ménard et al., 2019; Sacchetti et al., 2016). Since DNs also expressed *LTBR* (Figure 3C), we stimulated them after a short-term *in vitro* expansion with a combination of TNF/LT. Under TNF/LT activation, human DNs strikingly upregulated adhesion molecules (*ICAM1*, *VCAM1*), FRC specific factors (*CCL19, CCL21*, *IL7*), and *TNFSF13B,* while the pericytic markers *CSPG4* and *RGS5* were downregulated (Figure 3J). Altogether, our data argue for human DNs being tissue-specific perivascular precursors of lymphoid stromal cells.

Human immunologically-competent FRCs support T cell and B cell survival

In order to further characterize PDPN LSCs, we first applied Uniform Manifold Approximation and Projection (UMAP) dimensionality reduction on publicly available scRNA-seq data obtained from mouse LN LSCs (Rodda et al., 2018). These data were overlaid with the gene expression specific signatures of human native DNs, FRCs, and FDCs defined by our RNA-seq profiling (Figure 4A and Figure S4A). Our FRC-specific signature (Figure 2E) highlighted the 7 murine FRC clusters and excluded PvC and FDC clusters suggesting that we captured resting and activated FRC heterogeneity in the absence of DN and FDC contamination.

FRCs construct a unique reticular conduit network delivering small antigens to the cortex and organized as a collagen-rich core enveloped by a microfibrillar zone forming a basement membrane ensheathed by FRCs. In agreement, human FRCs shared with DNs a high expression of Collagen I, III, V, XII, XIV, XV, XVIII (Table S1 and Figure S4B). Moreover, human FRCs specifically produced large amounts of small leucin-rich proteoglycans, including decorin (*DCN*), fibromodulin (*FMOD*), osteomodulin (*OMD*), lumican (*LUM*) and podocan-like protein 1 (*PODNL1*), known to regulate matrix and elastic fiber assembly (Figure 4B). FRCs also overexpressed *LOXL1,* and *LOXL4* members of the lysyl oxidase family involved in the crosslinking of collagen and elastin, and *MFAP2, FBLN2, HMCN2*, and *EFEMP1/FBLN3*, four other ECM protein-bridging

factors, thus contributing to ECM stiffness and mechanical properties. Finally, matrix metalloproteinases (MMP), which are crucial for the extensive turnover of the ECM required to accommodate expansion and contraction of SLOs during immune response, were highly expressed by FRCs (Table S1 and Figure S3). As a whole, these data depicted the complete picture of conduit structure and ECM organization and maintenance created by pure native immunologically-competent FRCs.

Human FRCs expressed high amounts of *THBD* and *JAM2*, two markers previously described as highlighting chemokine-producing mouse FRCs (Frontera et al., 2011) (Figure 4B). In agreement, FRCs produced high amounts of *CCL19, CCL21* (Figure 3C) and *CXCL13,* together with factors involved in T cell and B cell survival, namely *IL7* and *BAFF*, and the alarmin *IL33* (Figure 4B). The expression of both CCL21 and CXCL13 by Transglutaminase-expressing FRCs was confirmed by immunohistofluorescence, highlighting a discrete population of $CXCL13^+$ FRCs around follicles (Figure 4C). We thus evaluated how human FRCs might promote the survival of naive B and T cells. We used $CD49a^-$PDPN LSCs as a control, since these cells shared FRC basic phenotype (Figure S4C) but were devoid of *TNFRSF13* and *IL7* expression (Figure 2). *In vitro* coculture experiments revealed a higher number of viable tonsil-derived naive $CD4^+$ T cells and $CD20^+$ B cells after 7 days in the presence of $CD49a^+$PDPN LSCs compared to $CD49a^-$PDPN LSCs (Figure 4D). Such T cell and B cell pro-survival activity is related in mouse stromal cells to the production of IL-7 (Link et al., 2007) and BAFF (Cremasco et al., 2014), respectively. These data argue for a key role of human $CD49a^+$PDPN LSCs as functional FRCs involved in B and T cell homeostasis.

Human FDC profile suggests active response to B cell and non-B cell stimuli

The GEP of a pure FDC population is yet to be established, due to the difficulty of isolating these very rare cells that are firmly associated with GC B cells. In the FDC signature, we first identified a strong upregulation of genes involved in the response to external stimuli (Figure 5a). In particular, FDCs expressed *CSF2RA, CSF2RB*, and *FGFR2,* revealing the capacity of FDCs to respond to GM-CSF and FGF. Moreover, FDCs expressed receptors involved in the crosstalk with Tfh. In particular, *IL21R* and *IL4R* are the receptors for the two main Tfh-derived cytokines (Crotty, 2019). Moreover, the poliovirus receptor (*PVR*) is involved in the adhesion and activation of $TIGIT^+$ Tfh (Boles et al., 2009; Godefroy et al., 2015) and is able to transduce a cell-intrinsic

reverse signal promoting adhesion, migration, proliferation, and survival (O'Donnell et al., 2019). Human FDCs also overexpressed *TLR4*, that triggers murine FDC maturation and cytokine production (Garin et al., 2010; Suzuki et al., 2010). Finally, *TNFRSF14*, a member of the TNF superfamily sharing with LTβR the capacity to interact with LIGHT and activate NF-κB pathway, was also strongly expressed by FDCs. The overexpression of *FGFR2, IL21R, IL4R*, and *TLR4* on human FDCs was confirmed at the single-cell level (Figure 5B).

As the most transcriptionally distinct LSC subset, FDCs expressed a specific pattern of transcription factors, including *SOX8* and *SOX9*, previously reported in mouse FDCs (Rodda et al., 2018), but also *FOXP4*, whose nuclear expression in CD21 FDCs was confirmed *in situ* and *ex vivo* on FDC-enriched cells (Figure 5C and Figure S5). FOXP4 favors cell survival (Wu et al., 2019), suggesting specific mechanisms regulating the long-term persistence of FDCs. Accordingly; the Bcl-2 family members were finely regulated in FDCs with a significantly lower level of *BCL2* and higher level of *BCL2A1*, a known NF-κB target gene (Figure 5C).

FDCs are known to support GC reaction and besides the well-defined FDC markers related to antigen presentation, including *CR1, CR2, FCAMR, FCER2, ICAM2,* and *CSTA* (Table S1), FDCs expressed high levels of *TNFRSF9*, *PTGIS*, *PTGES2, WNT5A, and DLL1*, which are all involved in GC B cell survival, proliferation, and differentiation (Jini Kim et al., 2013; Jungtae Kim et al., 2012; Middendorp et al., 2009; Yoon et al., 2009). FDCs overexpressed several immunosuppressive molecules including *CD200*, *IL4I1*, and *CD274* that could restrain T cell activation and proliferation, and increase GC response stringency (Figure 5D). Finally, FDCs are supposed to regulate the GC B cell response through the production of chemotactic molecules. Human purified FDCs exhibited the highest level of *CXCL13* whose migratory activity is enhanced by the FDC-specific soluble molecule FDC-SP (Al-Alwan et al., 2007), and the lowest level of *CXCL12* (Figure 5E and 4B). Conversely, FRCs overexpressed *CXCL12* as well as *CXCL14*, another CXCR4 ligand with synergistic activity with CXCL12 (Collins et al., 2017). In addition, analysis of human FDCs confirmed the current model of regulation of follicular B cell guidance through gradients of lipid mediators (Lu and Cyster, 2019). FDCs repressed *CH25H*, the rate limiting enzyme in the synthesis of the EBI2 ligand 7α,25-dihydroxycholesterol (7α,25-HC), known to guide the movement of recently activated B cells in interfollicular regions (Lu

and Cyster, 2019). Moreover, FDCs displayed low expression of *SPNS2*, involved in the secretion of sphingosine-1 phosphate (S1P), and high expression of *GGT5*, triggering the degradation of S-geranylgeranyl-L-glutathione (GGG) thus contributing to a higher level of S1P and GGG in the outer follicle and a confinement of GC B cells in the follicle center through the triggering of the inhibitory receptors S1PR2 and P2RY8. Altogether, we provide a comprehensive picture of FDC GEP, shedding light on the mechanisms of FDC-GC B cell crosstalk under steady-state conditions.

Malignant FL B cells and FL-LSCs are engaged in a bidirectional crosstalk

FL is the best paradigm of a malignancy dependent on a preserved lymphoid microenvironment harboring a retained follicular pattern (Lamaison and Tarte, 2019). Moreover, FRC-like cells obtained by *in vitro* differentiation of mesenchymal precursors support FL B cell growth (Amé-Thomas et al., 2007). We thus decided to evaluate the capacity of malignant FL B cells to specifically interact with LSC subsets by combining transcriptomic data previously obtained from purified FL B cells (Desmots et al., 2019) and our RNA-seq data from purified native human LSCs. This analysis was performed using the CellPhoneDB repository making it possible to study biologically relevant ligand-receptor interactions in order to infer cell-cell communication networks. When we defined the interactome between FL B cells and LSC subsets, a higher number of bidirectional interactions were predicted to occur between lymphoma cells and FRCs compared to FDCs (Figure 6A). DNs exhibited lower capacity to interact with FL cells than mature LSCs.

To further explore the lymphoma-supportive capacity of FRCs we evaluated their functional impact on the survival of purified FL B cells (n=8) using CD49a^{-}PDPN LSCs as a control (Figure 6B). Whereas CD49a^{-}PDPN LSCs have a limited impact on FL B cell survival *in vitro*, FRCs strongly increased the number of viable FL B cells at day 7. This activity was restricted to malignant B cells since FRCs were not able to support survival of normal GC B cells. These data suggest that, even if FL B cells display a GEP very close to that of normal centrocytes, they also exhibit specific capacities to interact with surrounding stromal cells. FL-FRCs and FL-FDCs display poorly characterized phenotypic changes that could impact their crosstalk with FL cells (Pandey et al., 2017). After checking that CD49a expression on FL-LSCs mimicked that of SLO LSCs (Figure S6A), we characterized FL-LSC subsets using RNA-seq of isolated FL-DNs (n=4), FL-FRCs (n=4), and FL-FDCs (n=3). An unsupervised PCA

revealed that FL-LSCs were first segregated according to their differentiation stage (Figure 6C). However, each FL-LSC subset also exhibited a distinct GEP compared to its normal counterpart as highlighted by the second PCA axis, a result confirmed by a Pearson correlation analysis (Figure 6D).

We next defined the FL-LSC signature by merging the genes differentially expressed between the three LSC subsets obtained from healthy donors and FL patients (943 genes, Figure 6E and Table S3, adjusted P-value < .01, fold-change>2). Using a list of genes upregulated in FL B cells compared to normal centrocytes (Desmots et al., 2019) (FL-B signature, Figure 6E, Table S4), we then applied NicheNet computational method to delineate the specific interactions underlying the crosstalk between FL-LSCs and FL B cells (Figure 6F). NicheNet incorporates, beyond ligand-receptor interactions, prior knowledge on intracellular signaling and resulting target gene regulation. This strategy could thus prioritize how sender cell ligands affect target genes in receiver cells. In addition, we used bootstrapping with randomized genes (1000 iterations) to estimate the p-value of each NicheNet-predicted active ligand to highlight the most significant crosstalk pathways (Figure 6G). We first defined FL-LSCs as sender cells and FL B cells as receiver cells (Figure 6F). Several chemokine-related pathways were found enriched at the interface between FL-LSCs and FL B cells (all with a P-value < .0001). Moreover, FL-FRCs and FL-FDCs overexpressed *CCL19*, *CCL21*, and *CXCL12* compared to FRCs and FDCs obtained from reactive SLOs and, simultaneously, FL B cells expressed higher levels of *CCR7* and *CXCR4* than normal CC (Figure S6B-C). Together with their reduced expression of the GC-confinement receptors *S1PR2* and *P2RY8,* and their increased expression of the *S1PR1* egress receptor (Figure S6D), these data suggested that FL B cells are prone to interact with FL-LSCs both within and outside follicles. Apart from chemokines, the analysis of the pathways specifically activated in FL B cells by FL-LSCs underlined a role for the TGF-β/BMP/activin signaling (P<.0001). In particular, we identified a simultaneous upregulation of *SMAD1*, *SMAD3*, the common signaling co-factor *SMAD4*, and the activin receptors *ACVR1*, *ACVR1B*, and *ACVR2B* compared to normal centrocytes (Figure S6E). To decipher how lymphoma cells could directly contribute to the modification of FL-LSC phenotype, we next evaluated the impact of FL B cells defined as sender cells on FL-LSCs considered as receiver cells (Figure 6f). Among the mechanisms of B cell dependent LSC polarization, TNF emerged as a key driver factor and we confirmed the upregulation of *TNF* and decreased expression of *LTA* in FL B

cells compared to CC (Pandey et al., 2017) whereas FL-FRCs overexpressed *TNFRSF1A* and *TNFRSF1B*, able to bind TNF but not LT (Figure S6F). FL B cells were also found to contribute to the activation of TGFβ signaling in FL-LSCs and interestingly, this hypothesis was reinforced by the identification of an upregulation of *TGFB1* and *INHBA* in FL B cells, whereas FL-FRCs and FL-FDCs overexpressed TGFβ receptors (Figure S6F-G). Our bootstrap strategy further confirmed that TNF and TGFβ signaling pathways were the most discriminant FL B cell-derived drivers of FL-LSC polarization ($P < .01$). Altogether we identified a combination of B cell-derived factors, including TNF/LT and TGF-β/INHBA that could contribute to the specific phenotype of FL-LSCs.

FL-DNs overexpressed several markers of mature LSCs including *PDGFRA, CCL19, CCL21, TNFRSF13B*, *VCAM1, and SOX8* (Figure S6H). We thus compared the Euclidean distance between DNs and mature LSCs in normal and malignant settings and demonstrated that FL-DNs were significantly closer to both FL-FRCs and FL-FDCs than DNs to FRCs and FDCs (Figure 6H). In FL tissues, we cannot detect $TRANCE^+$ marginal reticular cells, one of the other proposed FDC precursors (Jarjour et al., 2014) (Figure S7). These data suggest that infiltration by malignant FL B cells triggers early LSC reprogramming towards cancer-supportive CAFs.

TGF-β contributes to FL-LSC commitment in situ

To further evaluate the role of TNF and TGF-β in FL-LSC polarization, we performed *in vitro* stimulation of purified DNs for 3 days (n=5, Figure 7A). TNF/LT and TGF-β synergized to induce FL-LSC markers, including the chemokines *CXCL12, CCL19*, and *CCL2*, the adhesion molecules *ICAM2* and *VCAM1*, and *TNFRSF13B*. *CCL19* expression was also increased in FRCs stimulated *in vitro* by TNF/LT + TGF-β (Figure 7B, n=7). We then explored the relevance of these observations *in situ* in FL patients. For that purpose, we analyzed RNA-seq data obtained from fresh-frozen tumor biopsies of a cohort of 148 untreated patients with high-tumor-burden FL (PRIMA trial, NCT00140582) (Huet et al., 2018b). A significant correlation between *CCL19* and both *TGFB1* and *LTB* levels was identified, suggesting again that TNF/LT and TGF-β could contribute to the overexpression of CCL19/CCL21 in FL (Figure 7C). We next analyzed tumor microarrays obtained from 115 untreated patients with low-tumor-burden FL (FLIRT trial, NCT02303119) for CCL21 and CD21 expression by multiplex

immunohistofluorescence. In this cohort of early FL, 37% of patients retained an intact dense FDC network, whereas about 16% were completely devoid of FDC; the remaining 47% harboring a disrupted FDC organization (Figure 7D). We highlighted elevated CCL21 expression in FL compared to tonsils (n=18, Figure 7E). Moreover, a careful analysis of CCL21 expression revealed, besides a very bright staining of FL-FRCs, a specific expression of CCL21 by $CD21^+$ FL-FDCs (Figure 7F-G), thus confirming our transcriptomic data (Figure S6B). Collectively, these data support a role for TNF/LT and TGF-β in the crosstalk between FL B cells and FL-LSCs and confirmed the modification of FL-LSC functional properties *in situ*.

DISCUSSION

$CD31^-$ LSCs are paramount to maintain SLO structural integrity and support adaptive immune response (Krishnamurty and Turley, 2020). Our data provide a thorough characterization of human LSC subsets, making it possible to analyze LSC alterations, or ectopic induction of LSC-like cells, in pathological contexts. In particular, we identified CD49a, an integrin expressed on human clonogenic pluripotent BM-MSCs (Gindraux et al., 2007), as a marker of functional LSCs. CD49a expression highlighted perivascular DN cells with molecular, phenotypic, and functional features of human LSC precursors. CD49a also identified cytokine/chemokine-producing human FRCs within inflamed SLOs. At least 5 FRC subsets are identified within mouse LNs as highlighted by scRNA-seq analysis (Rodda et al., 2018). Analysis of *Cd49a/Itga1* expression in the *gp38*$^+$ fraction of these murine FRC subsets revealed a huge variability with no significant difference in the chemokine/cytokine gene expression pattern between *Cd49a*$^+$ and *Cd49a*$^-$ cell subsets (data not shown). Cd49a/Itga1 expression seems thus not able to distinguish immunologically-competent LSC subsets in mouse.

We also provided a deep GEP of mature FDCs. FDCs expressed a specific pattern of apoptosis regulators, in agreement with their unique capacity to retain and present intact antigens to B cells for extended periods(Heesters et al., 2014). Moreover, human FDCs expressed numerous receptors involved in the sensing of their surrounding microenvironment and the control of GC response fitness. Besides FDCs, other murine LSC subsets underpin B cell movement and survival, establishing a panel of B cell interacting LSCs defined by their expression of CXCL13 (Cremasco et al., 2014; Pikor

et al., 2020). Similarly, both FDCs and perifollicular FRCs expressed CXCL13 and TNFSF13B in human SLOs. Normal B cells and LSCs are engaged in a bidirectional crosstalk. The production of TNF and LT by GC B cells is required for proper FDC development and maintenance, and is closely dependent on FDC-derived CXCL13 (Ansel et al., 2000; Endres et al., 1999). Moreover, IL-4R-expressing B cells promote FRC proliferation and activation, whereas B cells sustain prolonged LSC remodeling after infection (Dubey et al., 2016; 2019; Gregory et al., 2017). FL B cells are characterized by a $TNF^{hi}LT^{lo}$ profile compared to normal CC, sustaining the progressive disappearance of phenotypically mature FDCs (Chang et al., 2003; Pandey et al., 2017; Pepe et al., 2018). Furthermore, FL B cells disseminate outside follicles, thus contacting directly the various LSC subsets with putative impact on whole stroma reprogramming. In agreement, our interactome analysis predicted a preferential interaction of FL B cells with FRCs, unlike FDCs. Together with the identification of ectopic FDC-like cells within FL B cell aggregates in invaded bone marrow (Pandey et al., 2017), these data could support the hypothesis of a strong dependency towards FDC network in the early stage of the disease or upon arrival of FL B cells in a non-lymphoid microenvironment, whereas FDCs become dispensable for later stages of FL progression, as recently proposed in chronic lymphocytic leukemia (CLL) (Heinig et al., 2014). The lack of cells expressing classical markers of marginal reticular cells within FL tissues raised the hypothesis of their differentiation into FDCs in response to chronic activation.

Based on the purification of the three main LSC subsets, we were able to draw a picture of the stromal landscape in FL, highlighting major qualitative changes in FDCs, FRCs, and LSC precursors associated with their conversion to CAFs. Chemokines were strongly deregulated and, besides the already-described CXCL12 induction, CCL19 and CCL21 were also found upregulated in FL-LSCs, unlike CXCL13. Moreover, we confirmed in untreated early FL patients that CCL21 was upregulated in FL-LSCs *in situ*, including in FL-FRCs and FL-FDCs. Conversely, in CLL, tumor B cells directly trigger aberrant CXCL13 expression in non-FDC infiltrating stromal cells, through LTβ-receptor activation and retinoic acid signaling (Farinello et al., 2018; Heinig et al., 2014), demonstrating the specificity of tumor cell-stromal cell crosstalk. The relevance of these observations is sustained by the demonstration that, in turn, FL B cells exhibited a $CXCR4^{hi}CCR7^{hi}S1PR1^{hi}$ $S1PR2^{lo}P2RY8^{lo}$ phenotype compared to normal CC, supporting their disseminated profile and preferential capacity to interact with

converted CAFs. The genes coding for the GC-confinement receptors *S1PR2* and *P2RY8*, as well as their signaling molecule *GNA13*, are frequently mutated in transformed FL and GC-like diffuse large B cell lymphomas (Muppidi et al., 2014). Our demonstration that this pathway is also affected in early FL reinforces the role of G-protein-coupled receptors in GC-derived lymphomas. Another interesting observation was the bidirectional implication of the TGFβ family. In solid cancers, TGFβ signaling activates CAFs, synergizing with NF-κB triggering by inflammatory stimuli, and is produced by CAFs to modulate tumor phenotype (Sahai et al., 2020). In FL, SMAD1 is upregulated and activated in malignant B cells (Munoz et al., 2004) and expression of TGF-β by LN FL B cells is involved in the alteration of intratumoral T cell function (Z.-Z. Yang et al., 2014; 2013). Moreover, FL tumor niche GEP is enriched for gene networks related to TGF-β signaling (Pangault et al., 2020), whereas TGF-β could contribute to the priming, by FL B cell-derived extracellular vesicles (EVs), of BM-MSCs into tumor-supportive stromal niche (Dumontet et al., 2021). We identified here a correlation between *CCL21* and *TGFB1* levels in the PRIMA cohort, suggesting that TGF-β could also contribute to the stromal phenotype within FL LN. We cannot exclude that other cell subsets of FL tumor microenvironment contribute to TGF-β production and activation. In agreement, other components of FL cell niche participate in the reprogramming of infiltrating stromal cells. In particular, FL-Tfh overexpress TNF/LT but also IL-4 (Amé-Thomas et al., 2012), that triggers CXCL12 expression in FL-CAFs (Pandey et al., 2017). An additional unsolved question is whether CAF phenotype is instructed by oncogenic mutations within cancer cells. In particular, *TNFRSF14/HVEM* mutations, found in 40% of FL patients, favor activation of pro-tumoral $TNF^{hi}LT^{hi}$ Tfh, able to sustain directly malignant B cell growth, and to activate FRCs and FDCs (Boice et al., 2016). Conversely, *EZH2* mutations, occurring in 25-30% of FL patients, impair requirement for Tfh help, while driving expansion of GC B cells dependent on an intact FDC network (Béguelin et al., 2020). It is tempting to speculate that other recurrent genetic alterations affecting B-T crosstalk, including mutations of *CREBBP* (Green et al., 2015), *CTSS* (Bararia et al., 2020), or *RRAGC* (Ortega-Molina et al., 2019), would also impact FL-CAF features. However, numerous non-mutually exclusive genetic alterations coexist in FL, creating a dynamic mosaic of malignant B cell subclones, and making it difficult to conclude on the individual impact of each of them on microenvironment reprogramming. Despite this high level of potential heterogeneity,

we could identify some shared pathways in our limited series of patients, thus providing some clues for understanding lymphomagenesis and design new therapeutic strategies.

The targeting of pro-survival signals delivered by infiltrating stromal cells could sensitize tumor cells to chemotherapy in CLL and mantle cell lymphomas (Park et al., 2020). Moreover, standard immunochemotherapy regiments in FL are based on the recruitment and activation of anti-tumor immune cells, a process profoundly affected by stroma organization and activation (Salmon et al., 2012). Altogether, our study suggests that therapeutic targeting of CAFs or CAF functions in FL could be a valuable approach in this incurable malignancy.

LIMITATIONS OF THE STUDY

Despite elegant cell-fate mapping strategies, the identity, localization, and differentiation potential of mouse LSC progenitors remain controversial, and we cannot exclude that, besides DNs, other precursors exist within human SLOs or in the surrounding adipose tissue. Human tonsils are widely used as a normal counterpart for studying FL microenvironment, given their chronically inflamed profile, with similarly high amounts of GC B cells and Tfh compared to FL LNs (Pangault et al., 2010) and the presence of mature activated FDC and FRC networks. However, further studies using different sources of inflamed and non-inflamed SLOs will be required to characterize, through scRNA-seq and spatial transcriptomics, the whole spectrum of human LSC heterogeneity, looking for the various B cell interacting reticular cell subsets recently proposed in mice (Pikor et al., 2020). Finally, mechanistic insights into the role of TNF and TGF-β pathways in FL-CAF polarization would require the use of mouse models allowing cell tracing and cell targeting. However, existing FL mouse models recreate single alterations in B cells and mimic only the early stage of the disease. Detailed analysis of LSCs obtained from large numbers of patients accounting for FL mutational landscape is highly challenging but would allow to definitively correlate FL stroma functional features to FL B cell genetic background.

ACKNOWLEDGMENTS

This work is supported by the Fondation ARC pour la Recherche sur le Cancer (Grant PGA1 RF20170205386), the Institut National du cancer (INCA AAP PLBIO-17-06), the

Agence Nationale de la Recherche (ANR, ANR-16-CE15-0019-03), and the LLS (TRP 6593-20). L.V. is recipient of a doctoral fellowship from the Labex IGO. S.L. is supported by a Chair d'Excellence of the Fondation Rennes 1 and Labex IGO. F.M. is supported by research grants from La Ligue Régionale contre le Cancer. Immunofluorescence studies were performed on the Microscopy Rennes Imaging Center (MRic) and on the H2P2 platform, both members of the UMS 6480 Biosit and of the national infrastructure France-BioImaging supported by the ANR (ANR-10-INBS-04). Cell sorting was performed at the UMS 6480 Biosit CytomeTRI facility. High-throughput sequencing has been performed by the ICGex NGS platform of the Institut Curie supported by the grants ANR-10-EQPX-03 (Equipex) and ANR-10-INBS-09-08 (France Génomique Consortium) from the ANR, by the ITMO-CANCER, and by the SiRIC-Curie program (SiRIC Grant INCa-DGOS-4654). The authors are indebted to the Centre de Ressources Biologiques (CRB)-Santé (BB-0033-00056) of Rennes hospital for the processing of biological samples, Christophe Ruaux for providing tonsil samples, Erwan Flecher for providing normal bone marrow samples, and the LYSA-P for generating TMA from patients included in the FLIRT trial (NCT02303119) sponsored by the Lymphoma Academic Research Organisation (LYSA).

AUTHOR CONTRIBUTIONS

FM: designed and performed experiments, analyzed data, and contributed writing; DRou: analyzed data, and contributed writing; LV, RA, CP: generated transcriptomic data from stromal cells and B cells; CL, MS: analyzed the TMA from the FLIRT cohort; SH, GS: provided the RNA-seq data on the PRIMA cohort; CM, MG: provided technical assistance; SB, PL: run the RNA sequencing; FMG: provided knowledge on CAF; VS, BT, DRos, SL: analyzed data; GC: provided the TMA from the FLIRT trial; TF: provided samples and discussed results; KT: designed and supervised research, analyzed data, and wrote the paper.

DECLARATION OF INTERESTS

The authors declare no competing interests.

INCLUSION AND DIVERSITY STATEMENT

One or more of the authors of this paper self-identifies as an underrepresented ethnic minority in science. One or more of the authors of this paper self-identifies as a member of the LGBTQ+ community. One or more of the authors of this paper self-identifies as living with a disability.

FIGURES LEGENDS

Figure 1. Human LSC subset identification

A) Gating strategy used for human tonsil LSCs. Three subsets were identified: $PDPN^+CD21^-$ (PDPN LSC, Purple), $PDPN^+CD21^+$ (CD21 LSC, Green), and $PDPN^-CD21^-$ (DN LSC, Red). Contour plot shows ICAM1 and VCAM1 expression on the 3 LSC populations.

B) Representative flow cytometry plots showing the expression of lymphoid stroma markers on the 3 LSC subsets**:** isotype control (red), expression of the corresponding marker (blue).

C) Human $CD21^-$ LSCs gated on CD49a including $CD49a^-$ PDPN LSC (Orange), $CD49a^+$ PDPN LSC (Blue), $CD49a^+$ DN LSC (Red), and $CD49a^-$ DN LSC (TN, Grey). Lymphoid stroma marker expression was evaluated and representative flow cytometry plots are shown**:** isotype control (red), expression of the corresponding marker (blue).

D) Immunofluorescence on tonsil sections for TGM2/Transglutaminase (Green) CD49a (Red), and CD21 (Blue). Nuclei were counterstained with SytoxBlue (White). Scale bar, 100µm. Boxes indicate areas magnified in right panels including GC (A) and extrafollicular zone (B) where scale bars represent 50µm.

See also Figure S1.

Figure 2. Transcriptomic characterization of human LSC subsets.

A) t-SNE analysis of single cell Q-PCR data obtained from the various purified LSC subsets ($CD49a^-$ PDPN LSC, n=29; $CD49a^+$ DN LSC, n=53; $CD49a^+$ PDPN LSC, n=79; CD21 LSC, n=47) computed on the 80-gene expression matrix.

B) Violin plot of LSC subset gene expression. Shown is the Log2-normalized expression scaled for each gene.

C-D GEP of human sorted LSCs including DNs (n=4), FRCs (n=5), and FDCs (n=4), was obtained by RNA-seq. Unsupervised analysis was performed by Principal Component Analysis (**C**), and by Pearson correlation matrix (**D**).

E) Differentially expressed genes represented through a Venn diagram.

F-G) GEP of human sorted LSCs were analyze by weight correlation network analysis (WGCNA). The relationship between the module eigengenes and the traits (LSC subsets) was evaluated based on a Mann-Whitney rank test and was represented as

a heat-map color-coded accordingly to the -LOG10(FDR) (**F**). The genes upregulated in the DN module (MEblue), FDC module (MEyellow), and FRC module (MEpink) were analyzed using Ingenuity Pathway Analysis. Shown are the top twenty pathways according to the p-value (**G**).

See also Figure S2, Figure S3, and Table S1.

Figure 3. Characterization of human DNs.

A) Localization of DNs was studied by immunohistofluorescence on tonsil sections. *Left*: alpha-smooth Muscle Actin (α-SMA, Green), CD31 (Red), CD146 (Blue) and Nucleus (White). White arrow indicates a perivascular cell co-expressing αSMA and CD146 but not CD31. *Right*: α-SMA (Green), CD146 (Red), CD49a (Blue) and Nucleus (White). White arrow indicates a triple positive cell co-expressing α-SMA, CD146, and CD49a. Scale Bars, 5µm.

B) DNs were evaluated for their clonogenic and differentiation potential. CFU-F were counted after 3 weeks of culture of DNs seeded in culture directly after sorting in 21% O_2 *versus* 1% O_2 (left, n=3 independent experiments). Adipocytic and osteoblastic differentiations were initiated after a short amplification of sorted DNs by seeding them in specific culture media for 3 weeks before staining by Oil Red O, revealing lipid droplets, and Alizarin Red, revealing calcium deposit.

C) Expression of DN-specific genes by the three LSC subsets as determined by RNA-seq analysis.

D) GEP of human sorted LSCs were combined with that of sorted BM-MSCs (n=4) obtained by RNA-seq. Unsupervised analysis was performed by Principal Component Analysis.

E) Euclidean distance between DNs and mature LSCs and between BM-MSCs and mature LSCs. ****P<. 0001

F) Scatter plot visualization of the PCA1 eigengene value of each stromal cell sample. *P<.05, **P<.01, ****P<.0001.

G) GSEA enrichment plots of the TNF/LT signature (Dumontet et al., 2021) in the genes ranked alongside the PCA1 axis.

H) Enrichment for transcription factor (TF) targets in the Top 5% genes positively driving PCA1 as determined with the TRRUST V2 database.

I) Expression of LSC markers by DNs and BM-MSCs as determined by RNA-seq analysis. * *P* < .05; ****P<.0001.

J) Effect of TNF/LT treatment on DNs (n= 5). DNs amplified for 10 days in culture were stimulated or not (medium) by TNF/LT for 7 days before analysis of the expression of markers related to lymphoid stroma or mesenchymal precursors by Q-PCR. The arbitrary value of 100 was assigned to unstimulated DNs. ** *P* < .01

See also Table S2.

Figure 4. Characterization of human FRCs

A) Comparison between human and mouse LSC subsets. Mouse scRNA-seq data (Rodda et al., 2018) were reanalyzed by UMAP and compared to our human RNA-seq data. FDC-specific, FRC-specific, and DN-specific gene signatures were highlighted on the UMAP.

B) Expression of FRC-specific genes by the three LSC subsets as determined by RNA-seq analysis (all *P* <.05).

C) Tonsil section was stained for CCL21 (Green), CXCL13 (Red), and Transglutaminase (Blue). Nuclei were counterstained with SytoxBlue (White). Scale Bar, 100µm. Box indicates the T/B border area with higher magnification (scale bar, 20µm).

D) Purified naive $CD4^+$ T cells (left) and naive B cells (right) were co-cultured for 7 days in the presence or not (medium) of $CD49a^+$ $PDPN^+$ LSCs (FRCs) or $CD49a^-$ $PDPN^+$ LSCs before counting the $DAPI^-$ viable lymphocytes by flow cytometry. Colors represent paired independent experiments (n= 6). * *P* < .05.

See also Figure S4.

Figure 5. Characterization of human FDCs

A) Expression of FDC-specific genes related to response to external stimuli by the 3 LSC subsets as determined by RNA-seq analysis.

B) Relevant genes were validated by Q-PCR at the single-cell level in sorted FDCs. Shown is the Log2-normalized expression scaled for each gene (all *P*<.05).

C) Expression of FDC-specific genes related to transcription factors or apoptosis regulation by the three LSC subsets as determined by RNA-seq analysis (all *P*<.05). Tonsil sections were stained for Transglutaminase (Green), FOXP4 (Red), and CD21L (Blue). Nuclei were counterstained with SytoxBlue. Scale bar, 100µm.

D) Expression of FDC-specific genes related to immunomodulatory molecules by the three LSC subsets as determined by RNA-seq analysis (all *P* <.05).

E) Expression of FDC-specific genes related to B cell migration by the three LSC subsets as determined by RNA-seq analysis (all *P* <.05).

See also Figure S5.

Figure 6. Interactions between FL B cells and LSCs.

A) Heatmap showing the number of bidirectional interactions between FL B cells and LSC subsets as evaluated using the CellPhoneDB repository to combine RNA-seq data from human LSCs and from published microarray data from FL B cells(Desmots et al., 2019).

B) FL B cells or GC B cells were co-cultured for 7 days or 2 days respectively in the presence or not (medium) of $CD49a^{+}$ $PDPN^{+}$ LSCs (FRCs) or $CD49a^{-}$ $PDPN^{+}$ LSCs before counting the number of $DAPI^{-}$ viable lymphocytes by flow cytometry. Colors represent independent experiments (n= 8). * *P* < .05, ** *P* < .01.

C) Principal component analysis obtained by RNA-seq analysis of purified DNs, FRCs, and FDCs obtained from tonsils in FL samples.

D) Pearson correlation matrix of RNA-seq data obtained from tonsil-LSCs and FL-LSCs.

E) Venn diagrams indicating the number genes differentially expressed in at least one comparison of LSC subsets purified from tonsils *versus* FL samples as evaluated by RNA-seq data, and the number of genes differentially expressed between purified FL B cells *versus* centrocytes (CC) as evaluated by microarray data.

F) Circos plots showing predicted interactions between FL B cells and FL-LSCs. On the left, FL-LSCs were defined as senders and FL B cells as receivers. On the right, FL B cells were defined as senders and FL-LSCs as receivers.

G) Bootstrapping with randomized genes (1000 iterations) to estimate the p-value of each NicheNet-predicted interaction, represented as a heatmap of-LOG10(pvalue).

H) Euclidean distance between DNs and FRCs and between DNs and FRCs in normal and FL settings. ***P<0.001, ****P<. 0001.

See also Figure S6, Figure S7, Table S3, and Table S4.

Figure 7. FL-LSC commitment *in situ*

A) DNs amplified for 10 days in culture were stimulated or not (CTR) for 3 days by TGF-β, TNF/LT, or a combination of TGF-β/TNF/LT before assessment of FL-LSC commitment by QPCR. Data were represented as a mean of 5 individual experiments.

B) FRCs (n=7) amplified for 10 days in culture were stimulated or not (CTR) for 3 days by TGF-β, TNF/LT, or a combination of TGF-β/TNF/LT before quantification of *CCL19* expression by QPCR.

C) The level of *CCL21* was correlated with that of *TGFB1, LTB,* and *TNF* evaluated in bulk RNA-seq from fresh-frozen tumor biopsies of 148 patients with high-tumor-burden FL. Shown is linear regression and p-value.

D) FDC patterns were classified according to the expression of CD21 by immunohistofluorescence. FL tissue sections were stained for CCL21 (Red) and CD21 (White). Nuclei were counterstained with DAPI (Blue). Scale Bar, 250µm. The FDC network was classified a TMA with 115 low-tumor-burden FL samples depending on the network integrity: dense, disrupted, and absent.

E) Quantification of CCL21 expression on FL LN and tonsil sections. *Left*: tissue sections were stained for CCL21 (Red) and CD21 (Green). Nuclei were counterstained with DAPI (Blue). Scale Bar, 250µm. *Right*: cumulative analysis of the CCL21 expression on a TMA with 115 low-tumor-burden FL samples compared to 18 tonsils. Shown is mean +/- SD. *** $P < .001$

F-G) Analysis of the colocalization between CCL21 (Red) and CD21 (Green) staining on a FL section (**F**) and a tonsil section (**G**). Scale Bar, 250µm. Boxes represent a higher magnification (scale bar, 50µm). The white color indicates the colocalization between CCL21 and CD21 to the related boxes.

STAR METHODS

Resource Availability

Lead contact. Further information and requests for resources and reagents should be directed to and will be fulfilled by the Lead Contact, Karin Tarte (karin.tarte@univ-rennes1.fr)

Materials availability. This study did not generate new unique reagents.

Data and code availability. The datasets generated during this study are available under GEO accession number GSE148656.

Experimental Models and Subject Details

Human subjects and samples. Patients were recruited under institutional review board approval following informed consent process according to the declaration of Helsinki and the French National Cancer Institute ethic committee recommendations. Tissue samples included tonsils collected from routine tonsillectomy, reactive LNs with follicular hyperplasia, LNs from FL patients, and BM from patients undergoing cardiac surgery. Human native BM-MSCs were sorted as previously described and immediately used for RNA extraction (Ménard et al., 2019). For functional assays, FL B cells were purified using the B Cell Isolation Kit II (Miltenyi Biotec), whereas tonsil GC B cells were first enriched by the B Cell Isolation Kit II before purification by anti-CD10 antibody (Immunotech) and anti-mouse IgG microbeads (Miltenyi Biotec). Tonsil naive B cells were purified using the Naive B Cell Isolation Kit II, and tonsil naive $CD4^+$ T cells using the Naïve CD4 T Cell Isolation Kit II (Miltenyi Biotec). All immune cell purifications were performed on an autoMACS Pro separator (Miltenyi Biotec) and purity of resulting populations was >98%. Tissue microarrays were obtained from a series of 115 early FL patients included in the FLIRT clinical trial (NCT02303119) sponsored by the Lymphoma Academic Research Organization (LYSA).

Method Details

Preparation of tonsil stromal cell subsets. Fresh tonsil tissue was cut in $3mm^3$ cubes that were incubated during 20 minutes at 37°C in dissociation buffer (DB) containing α-MEM supplemented with 10U/mL DNase (Roche), 200U/mL Collagense IV (Worthington), 1.6 U/mL Dispase (Worthington), and 5mM $MgCl_2$. Mechanical

dissociation was applied on a GentleMACS Dissociator (Miltenyi Biotec). A second round of 40-minute dissociation at 37°C in fresh DB with a 350 rpm agitation was performed. After enzymatic dissociation, the cell suspension was filtered on a 100µm cell strainer (Fisherbrand), and washed with washing buffer (WB) containing PBS supplemented with 1% Human serum albumin (HSA) and 0.6% of Sodium Citrate. Red blood cells were lyzed using EasyLyse solution (Dako) before two additional washes with WB. For flow cytometry characterization, cells were resuspended in WB containing DAPI (0.5 mg/mL) and directly stained before acquisition on a Beckman Coulter Gallios and analysis using FlowJo (v10.4). The detailed list of antibodies used for flow cytometry is provided in the Key Resources Table. The CD45/CD11b/CD235a/EPCAM/CD31-negative fraction was defined as LSCs. For cell sorting experiments, stromal cells were first enriched by depleting $CD45^+$ hematopoietic cells using CD45 Dynabeads (Thermo Fischer). Cells were then stained with a backgating cocktail (CD45/CD11b/CD235a/EPCAM/CD31), CD49a, PDPN, and CD21 antibodies for 20 minutes at 4°C. Importantly, the anti-CD21 antibody used is specific for the long isoform of CD21 (CD21L), which is expressed only by FDC unlike B cells (Liu et al., 1997). After washing, cells were filtered on a 70µm cell strainer and resuspended in WB containing DAPI (0.5 mg/mL). Cell sorting was performed on a FACSAria II (Becton Dickinson) using the 100µm nozzle. When indicated, FDCs were enriched after enzymatic dissociation for immunofluorescence. Tonsil cell suspension was centrifuged on a discontinuous Percoll gradient (Amersham) as previously described (Amé-Thomas et al., 2007). Briefly, the FDC-enriched fraction was collected from the interface of 15% and 25% layers, washed and resuspended in WB. Cell suspension was then incubated on a poly-L-lysine (Merck) precoated slice during 30 minutes at 37°c, and fixed with 4% paraformaldehyde (PFA, Merck) for 15 minutes.

Immunohistofluorescence. Human samples were embedded in Optimal Cutting Temperature Compound (OCT, Sakura) and frozen at -80°C. Cryostat sections (18µm thick) were fixed with 4% PFA for 10min before incubation for 1 hour with a blocking solution (PBS, 2% Bovine serum albumin, 4% donkey serum and 0.1% saponin). Slides were then incubated in a humidified chamber overnight at 4°C with primary antibodies. After washes in PBS/0.1% saponin, slides were incubated with corresponding secondary antibodies for 1 hour at RT. Finally, tissue sections were mounted with Mowiol (Merck) antifade reagent containing 20µM of SytoxBlue nucleic

acid stain (Thermo Fischer) and analyzed by confocal microscopy on a SP8 (Leica Microsystems). ImageJ software (National Institutes of Health) was used for image analysis. The list of primary and secondary antibodies used for immunohistofluorescence is provided in the Key Resources Table**.**

Real time quantitative PCR. RNA was extracted by using NucleoSpin RNA plus xs Kit (Macherey-Nagel) and gene expression level was assessed using the Fluidigm BioMark HD system. Briefly, cDNAs were obtained using the Fluidigm reverse transcription Master Mix and were then preamplified for 14 cycles in the presence Pre-Amp Master Mix and pooled Taqman assay mix. Gene expression was then measured with the Taqman Gene Expression Master Mix on a 96.96 Dynamic Array IFC. Expression level was calculated with the CT calculation method and RPLPO and RSP17 as housekeeping genes. The list of assay-on-demand used is provided in Supplemental Table S5.

Single Cell RT-QPCR. Single-cell experiments were performed using the Fluidigm C1 systems according to manufacturer instructions. Briefly, sorted stromal cells were captured with C1 integrated fluidic circuits (IFC) medium-cell (10-17µm) chips (Fluidigm). Cells were then lysed, and reverse transcription and pre-amplification was done within the C1 system. Gene expression was then assessed by qPCR with 80 selected Taqman assays and 3 housekeeping genes using the TaqMan Gene Expression Master Mix on a 96.96 Dynamic Array IFC and the Fluidigm BioMark HD system. After removal of cell outliers using the R package fluidigmSC (Fluidigm SINGuLAR Analysis Toolset, R package version 3.6.3), the gene expression profile of remaining cells was determined. The Raw Ct values were converted into expression level on a log2 scale. Significant genes were selected using an ANOVA with built-in module of the SINGuLAR Analysis Toolset package. The list of assay-on-demand used is provided in Supplemental Table S5.

RNA-seq analysis. Sorted tonsil FDCs (n=4), FRCs (n=5), DNs (n=4), sorted BM-MSCs (n=4), and sorted FL-FDCs (n=3), FL-FRCs (n=4), and FL-DNs (n=4) were used for RNA-seq analysis. RNA extractions were performed with the Single Cell RNA Purification Kit (Norgen Biotek, Canada). Library for RNA-sequencing was then prepared with the SMARTer Low Input RNA kit (Takara). After quality control, libraries

were sequenced with 2 x 100-bp paired-end reads on the Illumina Hiseq2500 sequencer generating more than 47 million reads per sample with > 80% of sequences achieving > Q30 Phred quality scores. Raw data were checked for quality using FastQC (v0.11.5) and aligned to the reference genome GRCh38 release 90 using STAR (v2.5.2) (Dobin et al., 2013). Read summarization, gene and transcript counts were performed using featureCounts (Liao et al., 2014) (version 1.5.0) from the Subread R package.

Colony-forming unit assays and in vitro differentiation. Sorted DNs were resuspended in α-MEM supplemented with 10% FCS (Hyclone), 100 IU/mL penicillin and 100 µg/mL streptomycin and seeded at 50 cells/cm^2 in 1% O_2 or 21% O_2. Fresh medium was replaced every week. After 3 weeks, cells were stained with May-Grunwald-Giemsa, and colonies with > 50 cells were counted. Each experiment was performed in triplicate. To evaluate the differentiation potential of DNs, sorted cells were first plated at 15000 cells/cm^2 in α-MEM supplemented with 10% FCS (Hyclone), 100IU/mL penicillin, 100µg/mL streptomycin and cultured in 1% O_2 during 10 days. For adipogenic differentiation, cells were then cultured in StemMACS AdipoDiff Media (Miltenyi) for 21 days before fixation and staining with Oil-red O (Sigma-Aldrich). Osteoblast differentiation was achieved after 21 days of culture in StemMACS OsteoDiff media (Miltenyi). Cells were then washed, fixed, and stained with Alizarin red (Sigma-Aldrich). For the differentiation of DNs toward FRC, cells were stimulated by TNF (10 ng/mL) and LT (100 ng/mL; R&D Systems) for 7 days. RNA was extracted followed by RT-qPCR using assay-on-demand primers for indicated genes. For differentiation of DNs and FRCs toward FL-LSC-like cells, DNs were stimulated by TGFβ (8 ng/ml; R&D Systems) alone or in combination with TNF and LT for 3 days. RNA was extracted followed by RT-qPCR using assay-on-demand primers for indicated genes.

***Cell survival assays*.** CD49a$^+$ PDPN LSCs and CD49a$^-$ PDPN LSCs were sorted and resuspended in α-MEM supplemented with 10% FCS (Hyclone), 100IU/mL penicillin, and 100µg/mL streptomycin at 15000 cells/cm^2 in a 96-well plate until confluence. After washing in PBS, naive B cells, naive CD4 T cells, GC B cells, and FL B cells were added at 150,000 cells/well in RPMI supplemented with 2% FCS (Thermo Fischer),

100 IU/mL penicillin, and 100 µg/mL streptomycin. After 2 days of culture for GC B cells or 7 days of culture for other immune cell types, the absolute number of $CD20^{+}DAPI^{-}$ viable B cells or $CD4^{+}DAPI^{-}$ viable T cells was quantified using Flow-Count beads (Beckman Coulter) by flow cytometry.

Analysis of TMA from FL patients. For multiplex fluorescence microscopy and analysis, 18 FFPE human tonsils and TMA of 115 patients with a follicular lymphoma from the FLIRT cohort (NCT02303119) were used. Four-micrometer-thick sections obtained with a microtome (Histocore multicut Leica) were transferred onto plus-charged slides (VWR international), followed by multiplex immunofluorescence staining with a U DISCOVERY 5 plex immunofluorescence (Roche Diagnostics). Two sequential rounds of staining were performed, each including heat deactivation step, followed by incubation with primary antibody and corresponding HRP secondary antibody. Staining for CCL21 (primary antibody from Biorad) and CD21 (primary antibody from Biotechne) were visualized on the same section. HRP enzyme mediated deposition of the tyramide coupled to respectively rhodamine and FAM corresponding species fluorophores (kit Ventana Medical Systems). After two sequential reactions, sections were counterstained with DAPI and coverslipped using Fluoromount (CliniSciences). Visualization was performed with the Nanozoomer (Hamamatsu Photonics) equipped with the multicolor fluorescence module. CCL21 detection and quantification was performed using an automated analysis by machine learning with the HALO software (Indicalabs). Four zones in each tonsil were quantified and the average was used for the comparison with FL patients. The FDC network pattern was classified by a certified pathologist as (1) absence; (2) disrupted: scattered or peripheral presence of FDC; (3) dense: almost all tumor follicles were packed by FDC. The colocalization between CD21 and CCL21 staining was evaluated using the plugin Colocalization Threshold in FIJI software.

Quantification and Statistical Analysis

RNA-seq analysis. Data normalization and differential gene expression were performed with the DESeq2 R package (v1.22.2). Significant genes were defined as $p < 0.01$ after adjustment for multiple testing by Bonferroni correction and used in downstream analysis. Euclidean distance was calculated using the R package stats

(v4.0.4) with the function dist. Pearson correlations were performed on the top 25% most variable genes. Correlation matrix were visualized using the heatplot() function of the made4 R package (v1.58.0). Principal Component Analysis (PCA) was done after scaling of the top 25% most variable genes, with the prcomp() function and visualized using the Factoextra R package (v1.0.7). Visualization of differentially expressed gene clusters was done using the heatplot function and Venn Diagrams.

Weighted Gene Correlation network analysis (WGCNA). We used the WGCNA R package (v1.68)(Langfelder and Horvath, 2008) to identify modules of co-expressed genes among the 13 tonsil LSC samples analyzed by RNA-seq. For this analysis, we retained the top 75% most variable genes. Expression matrix was log2 transformed and the network was constructed by Pearson correlation considering a soft threshold power(β) of 8 identified with the function Pick Soft Threshold. Then, a topological overlap metric (TOM) matrix was derived from the gene expression matrix and the dissimilarity of TOM was calculated. Hierarchical clustering tree was created and modules were generated by the dynamic tree cut method, with a minimum module size of 100 and a deepSplit of 2. Each module was marked by a color. In order to reduce the module numbers, modules with a similarity of more that 80% were merged with the MergedModule function and only 13 modules were used for subsequent analysis. The module eigengenes (ME) were then assigned to each cell types and visualized as a box-plot. To determine if co-expression modules were associated with LSC subtypes, we performed a Mann-Whitney test, and a heatmap visualization was then created and colored according to the -LOG10(padj), padj being the FDR-adjusted p-value (FDR: False Discovery Rate). Finally, module genelists were used for downstream enrichment pathway using the Ingenuity Pathway Analysis software (QIAGEN Bioinformatics).

Comparison with mouse LN stromal cell GEP. Raw microarray data corresponding to FRC and DN mouse skin-draining LNs were downloaded from the NCBI GEO database (GSE 15907)(Malhotra et al., 2012). Mouse gene symbols were mapped to human gene symbols using the BiomaRt R package (v2.40.5). GSEA preRanked analysis was conducted on the ranked gene lists generated for each pairwise comparison of stromal cell phenotypes, the ranking being based on the moderated t-test statistics (limma R package). Raw single cell RNA-seq data and clustering results

(*i.e* cell type annotation) from mouse lymph node stromal cells were downloaded from the NCBI GEO database (GSE112903)(Rodda et al., 2018) and UMAP dimensionality reduction was performed using the RunUMAP function of the Seurat package (v3.1.5), based on 10 aligned correlation components (Stuart et al., 2019). Clusters of genes up-regulated in DNs, FDCs, and FRCs computed from the RNA-seq data analysis were then used as signatures for geneset scoring. Gene names were converted to their mouse equivalent with a home-made R script and the homologene package. Signature scores were computed with the AddModuleScore function of the Seurat R package. This function calculates for each individual cell the average expression of each gene signature, subtracted by the aggregated expression of control gene sets. All the analysed genes were binned into 25 bins based on their averaged expression, and for each gene of the gene signature, 100 control genes were randomly selected from the same bin as the gene. For each gene signature, cell scores were visualized on UMAP and violin plots using Seurat and Vioplot (v0.3.0) packages respectively. Student's t tests were performed to calculate statistical significance between cell clusters with p-value adjustment by the FDR correction of Benjamini-Hochberg.

Interactome analysis. For interactome analysis, CellPhoneDB (v2.0) (Efremova et al., 2020) and Nichenet (v0.1.0) (Browaeys et al., 2020) scripts were used accordingly to author's recommendations. We first created a data matrix containing the RNA-seq data from the 13 tonsil LSC samples and the microarray data from 10 FL B cell samples, keeping all genes that were not shared between the two expression datasets. We then used the CellphoneDB python script with the following parameters: .8 for ratio of cell in a cluster, a p-value of .05, and a number of iterations of 1000. The numbers of significant interactions for which both a ligand and a receptor were present were then summarized for each cell type and direction (*eg.* stromal cells toward FL-B cells and FL-B cells toward stromal cells) and represented through a heatmap using the pheatmap R package.

In another approach, we used the Nichenet R package, to identify top ligand-receptor interactions between FL-LSCs and FL-B cells. RNA-seq from tonsil- and FL-LSCs were normalized and each FL-LSC subset was compared to its normal counterpart using Deseq2 R package, with significant genes defined as a fold change>2 and a $p < 0.01$ after adjustment for multiple testing by Bonferroni correction. Genes upregulated in at least one FL-LSC subset compared to its normal counterpart were keep for subsequent

Nichenet analysis. For B cells, differentially expressed genes were obtained from microarray data already published (purified centrocytes, GSE136248, n=5; purified FL B cells, GSE85233, n=10) after limma analysis with a FDR of 5% and a fold change>1.5. Upregulated genes in each cell type were then used to infer active ligand-target links using NicheNet algorithm. An expression table was created by merging gene expression in B cells and LSC in HD and FL contexts. Expressed genes were then defined in sender and receiver cells based on an average log2 expression above 7.5 in LSC samples and 4 in B cell samples. Genesets of interest (upregulated genes in FL condition compared to the healthy condition) were used to predict how ligands can impact target genes and ranked receptors accordingly to their activity. Then the best upstream ligands were filtered by the genes that were expressed in sender cells. In addition, we used a bootstrap test with 1000 random gene permutations (among the receiver-expressed genes) to create a distribution of each ligand activity and estimate a P-value for each NicheNet observed activity. Ligand-target interactions were represented through Circos visualizations (R circlize package v0.4.9) with the best upstream ligands.

Analysis of RNA-seq from FL patients. Normalized counts from RNA-seq data of a cohort of 148 untreated patients with high-tumor-burden FL enrolled in the phase 3 randomized PRIMA trial (Huet et al., 2018b) were used to perform correlation analysis with selected target genes. Correlation tests were performed with the rcorr function from the Hmisc R (v1.0.0) package.

Statistical analysis

Statistical analyses were performed with Prism software version 8.3.1 (GraphPad Software) using the non-parametric Wilcoxon signed-rank test for paired samples, the non-parametric Mann-Whitney test for independent samples, or one-way Anova whenever appropriate.

Additional Resources

The PRIMA trial and the FLIRT trial are registered at ClinicalTrial.gov (NCT00140582 and NCT02303119; respectively).

REFERENCES

Al-Alwan, M., Du, Q., Hou, S., Nashed, B., Fan, Y., Yang, X., Marshall, A.J., 2007. Follicular dendritic cell secreted protein (FDC-SP) regulates germinal center and antibody responses. J. Immunol. 178, 7859–7867. doi:10.4049/jimmunol.178.12.7859

Amé-Thomas, P., Le Priol, J., Yssel, H., Caron, G., Pangault, C., Jean, R., Martin, N., Marafioti, T., Gaulard, P., Lamy, T., Fest, T., Semana, G., Tarte, K., 2012. Characterization of intratumoral follicular helper T cells in follicular lymphoma: role in the survival of malignant B cells. Leukemia 26, 1053–1063. doi:10.1038/leu.2011.301

Amé-Thomas, P., Maby-El Hajjami, H., Monvoisin, C., Jean, R., Monnier, D., Caulet-Maugendre, S., Guillaudeux, T., Lamy, T., Fest, T., Tarte, K., 2007. Human mesenchymal stem cells isolated from bone marrow and lymphoid organs support tumor B-cell growth: role of stromal cells in follicular lymphoma pathogenesis. Blood 109, 693–702. doi:10.1182/blood-2006-05-020800

Amé-Thomas, P., Tarte, K., 2014. The yin and the yang of follicular lymphoma cell niches: role of microenvironment heterogeneity and plasticity. Semin. Cancer Biol. 24, 23–32. doi:10.1016/j.semcancer.2013.08.001

Ansel, K.M., Ngo, V.N., Hyman, P.L., Luther, S.A., Förster, R., Sedgwick, J.D., Browning, J.L., Lipp, M., Cyster, J.G., 2000. A chemokine-driven positive feedback loop organizes lymphoid follicles. Nature 406, 309–314. doi:10.1038/35018581

Armulik, A., Genové, G., Betsholtz, C., 2011. Pericytes: developmental, physiological, and pathological perspectives, problems, and promises. Dev. Cell 21, 193–215. doi:10.1016/j.devcel.2011.07.001

Astarita, J.L., Cremasco, V., Fu, J., Darnell, M.C., Peck, J.R., Nieves-Bonilla, J.M., Song, K., Kondo, Y., Woodruff, M.C., Gogineni, A., Onder, L., Ludewig, B., Weimer, R.M., Carroll, M.C., Mooney, D.J., Xia, L., Turley, S.J., 2015. The CLEC-2-podoplanin axis controls the contractility of fibroblastic reticular cells and lymph node microarchitecture. Nat. Immunol. 16, 75–84. doi:10.1038/ni.3035

Bahsoun, S., Coopman, K., Forsyth, N.R., Akam, E.C., 2018. The Role of Dissolved Oxygen Levels on Human Mesenchymal Stem Cell Culture Success, Regulatory Compliance, and Therapeutic Potential. Stem Cells Dev. 27, 1303–1321. doi:10.1089/scd.2017.0291

Bar-Ephraim, Y.E., Konijn, T., Gönültas, M., Mebius, R.E., Reijmers, R.M., 2016. A Reproducible Method for Isolation and In Vitro Culture of Functional Human Lymphoid Stromal Cells from Tonsils. PLoS ONE 11, e0167555. doi:10.1371/journal.pone.0167555

Bararia, D., Hildebrand, J.A., Stolz, S., Haebe, S., Alig, S., Trevisani, C.P., Osorio-Barrios, F., Bartoschek, M.D., Mentz, M., Pastore, A., Gaitzsch, E., Heide, M., Jurinovic, V., Rautter, K., Gunawardana, J., Sabdia, M.B., Szczepanowski, M., Richter, J., Klapper, W., Louissaint, A., Ludwig, C., Bultmann, S., Leonhardt, H., Eustermann, S., Hopfner, K.-P., Hiddemann, W., Bergwelt-Baildon, von, M., Steidl, C., Kridel, R., Tobin, J.W.D., Gandhi, M.K., Weinstock, D.M., Schmidt-Supprian, M., Sárosi, M.B., Rudelius, M., Passerini, V., Mautner, J., Weigert, O., 2020. Cathepsin S Alterations Induce a Tumor-Promoting Immune Microenvironment in Follicular Lymphoma. Cell Rep 31, 107522. doi:10.1016/j.celrep.2020.107522

Béguelin, W., Teater, M., Meydan, C., Hoehn, K.B., Phillip, J.M., Soshnev, A.A., Venturutti, L., Rivas, M.A., Calvo Fernández, M.T., Gutierrez, J., Camarillo, J.M., Takata, K., Tarte, K., Kelleher, N.L., Steidl, C., Mason, C.E., Elemento, O., Allis,

C.D., Kleinstein, S.H., Melnick, A.M., 2020. Mutant EZH2 Induces a Pre-malignant Lymphoma Niche by Reprogramming the Immune Response. Cancer Cell 37, 655–673.e11. doi:10.1016/j.ccell.2020.04.004

Bénézech, C., Mader, E., Desanti, G., Khan, M., Nakamura, K., White, A., Ware, C.F., Anderson, G., Caamaño, J.H., 2012. Lymphotoxin-β receptor signaling through NF-κB2-RelB pathway reprograms adipocyte precursors as lymph node stromal cells. Immunity 37, 721–734. doi:10.1016/j.immuni.2012.06.010

Boice, M., Salloum, D., Mourcin, F., Sanghvi, V., Amin, R., Oricchio, E., Jiang, M., Mottok, A., Denis-Lagache, N., Ciriello, G., Tam, W., Teruya-Feldstein, J., de Stanchina, E., Chan, W.C., Malek, S.N., Ennishi, D., Brentjens, R.J., Gascoyne, R.D., Cogné, M., Tarte, K., Wendel, H.-G., 2016. Loss of the HVEM Tumor Suppressor in Lymphoma and Restoration by Modified CAR-T Cells. Cell 167, 405–418.e13. doi:10.1016/j.cell.2016.08.032

Boles, K.S., Vermi, W., Facchetti, F., Fuchs, A., Wilson, T.J., Diacovo, T.G., Cella, M., Colonna, M., 2009. A novel molecular interaction for the adhesion of follicular CD4 T cells to follicular DC. Eur. J. Immunol. 39, 695–703. doi:10.1002/eji.200839116

Browaeys, R., Saelens, W., Saeys, Y., 2020. NicheNet: modeling intercellular communication by linking ligands to target genes. Nat. Methods 17, 159–162. doi:10.1038/s41592-019-0667-5

Chai, Q., Onder, L., Scandella, E., Gil-Cruz, C., Perez-Shibayama, C., Cupovic, J., Danuser, R., Sparwasser, T., Luther, S.A., Thiel, V., Rülicke, T., Stein, J.V., Hehlgans, T., Ludewig, B., 2013. Maturation of lymph node fibroblastic reticular cells from myofibroblastic precursors is critical for antiviral immunity. Immunity 38, 1013–1024. doi:10.1016/j.immuni.2013.03.012

Chang, K.-C., Huang, X., Medeiros, L.J., Jones, D., 2003. Germinal centre-like versus undifferentiated stromal immunophenotypes in follicular lymphoma. J. Pathol. 201, 404–412. doi:10.1002/path.1478

Cheng, H.-W., Onder, L., Novkovic, M., Soneson, C., Lütge, M., Pikor, N., Scandella, E., Robinson, M.D., Miyazaki, J.-I., Tersteegen, A., Sorg, U., Pfeffer, K., Rülicke, T., Hehlgans, T., Ludewig, B., 2019. Origin and differentiation trajectories of fibroblastic reticular cells in the splenic white pulp. Nat Commun 10, 1739–14. doi:10.1038/s41467-019-09728-3

Collins, P.J., McCully, M.L., Martínez-Muñoz, L., Santiago, C., Wheeldon, J., Caucheteux, S., Thelen, S., Cecchinato, V., Laufer, J.M., Purvanov, V., Monneau, Y.R., Lortat-Jacob, H., Legler, D.F., Uguccioni, M., Thelen, M., Piguet, V., Mellado, M., Moser, B., 2017. Epithelial chemokine CXCL14 synergizes with CXCL12 via allosteric modulation of CXCR4. FASEB J. 31, 3084–3097. doi:10.1096/fj.201700013R

Cremasco, V., Woodruff, M.C., Onder, L., Cupovic, J., Nieves-Bonilla, J.M., Schildberg, F.A., Chang, J., Cremasco, F., Harvey, C.J., Wucherpfennig, K., Ludewig, B., Carroll, M.C., Turley, S.J., 2014. B cell homeostasis and follicle confines are governed by fibroblastic reticular cells. Nat. Immunol. 15, 973–981. doi:10.1038/ni.2965

Crotty, S., 2019. T Follicular Helper Cell Biology: A Decade of Discovery and Diseases. Immunity 50, 1132–1148. doi:10.1016/j.immuni.2019.04.011

Denton, A.E., Carr, E.J., Magiera, L.P., Watts, A.J.B., Fearon, D.T., 2019. Embryonic FAP+ lymphoid tissue organizer cells generate the reticular network of adult lymph nodes. J. Exp. Med. 216, 2242–2252. doi:10.1084/jem.20181705

Desmots, F., Roussel, M., Pangault, C., Llamas-Gutierrez, F., Pastoret, C., Guiheneuf, E., Le Priol, J., Camara-Clayette, V., Caron, G., Henry, C., Belaud-Rotureau, M.-

A., Godmer, P., Lamy, T., Jardin, F., Tarte, K., Ribrag, V., Fest, T., 2019. Pan-HDAC Inhibitors Restore PRDM1 Response to IL21 in CREBBP-Mutated Follicular Lymphoma. Clin. Cancer Res. 25, 735–746. doi:10.1158/1078-0432.CCR-18-1153

Dobin, A., Davis, C.A., Schlesinger, F., Drenkow, J., Zaleski, C., Jha, S., Batut, P., Chaisson, M., Gingeras, T.R., 2013. STAR: ultrafast universal RNA-seq aligner. Bioinformatics 29, 15–21. doi:10.1093/bioinformatics/bts635

Dubey, L.K., Lebon, L., Mosconi, I., Yang, C.-Y., Scandella, E., Ludewig, B., Luther, S.A., Harris, N.L., 2016. Lymphotoxin-Dependent B Cell-FRC Crosstalk Promotes De Novo Follicle Formation and Antibody Production following Intestinal Helminth Infection. Cell Rep 15, 1527–1541. doi:10.1016/j.celrep.2016.04.023

Dubey, L.K., Ludewig, B., Luther, S.A., Harris, N.L., 2019. IL-4Rα-Expressing B Cells Are Required for CXCL13 Production by Fibroblastic Reticular Cells. Cell Rep 27, 2442–2458.e5. doi:10.1016/j.celrep.2019.04.079

Dumontet, E., Pangault, C., Roulois, D., Desoteux, M., Léonard, S., Marchand, T., Legoix, P., Loew, D., Dingli, F., Dulong, J., Flecher, E., Coulouarn, C., Cartron, G., Fest, T., Tarte K. 2021. Extracellular vesicles shed by follicular lymphoma B cells promote the polarization of bone marrow stromal cell niche. Blood online. doi: 10.1182/blood.2020008791

Efremova, M., Vento-Tormo, M., Teichmann, S.A., Vento-Tormo, R., 2020. CellPhoneDB: inferring cell-cell communication from combined expression of multi-subunit ligand-receptor complexes. Nat Protoc 15, 1484–1506. doi:10.1038/s41596-020-0292-x

Endres, R., Alimzhanov, M.B., Plitz, T., Fütterer, A., Kosco-Vilbois, M.H., Nedospasov, S.A., Rajewsky, K., Pfeffer, K., 1999. Mature follicular dendritic cell networks depend on expression of lymphotoxin beta receptor by radioresistant stromal cells and of lymphotoxin beta and tumor necrosis factor by B cells. J. Exp. Med. 189, 159–168.

Farinello, D., Woziński, M., Lenti, E., Genovese, L., Bianchessi, S., Migliori, E., Sacchetti, N., di Lillo, A., Bertilaccio, M.T.S., de Lalla, C., Valsecchi, R., Gleave, S.B., Lligé, D., Scielzo, C., Mauri, L., Ciampa, M.G., Scarfò, L., Bernardi, R., Lazarevic, D., Gonzalez-Farre, B., Bongiovanni, L., Campo, E., Cerutti, A., Ponzoni, M., Pattini, L., Caligaris-Cappio, F., Ghia, P., Brendolan, A., 2018. A retinoic acid-dependent stroma-leukemia crosstalk promotes chronic lymphocytic leukemia progression. Nat Commun 9, 1787. doi:10.1038/s41467-018-04150-7

Fletcher, A.L., Acton, S.E., Knoblich, K., 2015. Lymph node fibroblastic reticular cells in health and disease. Nat. Rev. Immunol. 15, 350–361. doi:10.1038/nri3846

Frontera, V., Arcangeli, M.-L., Zimmerli, C., Bardin, F., Obrados, E., Audebert, S., Bajénoff, M., Borg, J.-P., Aurrand-Lions, M., 2011. Cutting edge: JAM-C controls homeostatic chemokine secretion in lymph node fibroblastic reticular cells expressing thrombomodulin. J. Immunol. 187, 603–607. doi:10.4049/jimmunol.1003441

Garin, A., Meyer-Hermann, M., Contie, M., Figge, M.T., Buatois, V., Gunzer, M., Toellner, K.-M., Elson, G., Kosco-Vilbois, M.H., 2010. Toll-like receptor 4 signaling by follicular dendritic cells is pivotal for germinal center onset and affinity maturation. Immunity 33, 84–95. doi:10.1016/j.immuni.2010.07.005

Gil-Ortega, M., Garidou, L., Barreau, C., Maumus, M., Breasson, L., Tavernier, G., García-Prieto, C.F., Bouloumié, A., Casteilla, L., Sengenès, C., 2013. Native adipose stromal cells egress from adipose tissue in vivo: evidence during lymph node activation. Stem Cells 31, 1309–1320. doi:10.1002/stem.1375

Gindraux, F., Selmani, Z., Obert, L., Davani, S., Tiberghien, P., Hervé, P.,

Deschaseaux, F., 2007. Human and rodent bone marrow mesenchymal stem cells that express primitive stem cell markers can be directly enriched by using the CD49a molecule. Cell Tissue Res. 327, 471–483. doi:10.1007/s00441-006-0292-3

Godefroy, E., Zhong, H., Pham, P., Friedman, D., Yazdanbakhsh, K., 2015. TIGIT-positive circulating follicular helper T cells display robust B-cell help functions: potential role in sickle cell alloimmunization. Haematologica 100, 1415–1425. doi:10.3324/haematol.2015.132738

Green, M.R., Kihira, S., Liu, C.L., Nair, R.V., Salari, R., Gentles, A.J., Irish, J., Stehr, H., Vicente-Dueñas, C., Romero-Camarero, I., Sanchez-Garcia, I., Plevritis, S.K., Arber, D.A., Batzoglou, S., Levy, R., Alizadeh, A.A., 2015. Mutations in early follicular lymphoma progenitors are associated with suppressed antigen presentation. Proc. Natl. Acad. Sci. U.S.A. 112, E1116–25. doi:10.1073/pnas.1501199112

Gregory, J.L., Walter, A., Alexandre, Y.O., Hor, J.L., Liu, R., Ma, J.Z., Devi, S., Tokuda, N., Owada, Y., Mackay, L.K., Smyth, G.K., Heath, W.R., Mueller, S.N., 2017. Infection Programs Sustained Lymphoid Stromal Cell Responses and Shapes Lymph Node Remodeling upon Secondary Challenge. Cell Rep 18, 406–418. doi:10.1016/j.celrep.2016.12.038

Grégoire, M., Guilloton, F., Pangault, C., Mourcin, F., Sok, P., Latour, M., Amé-Thomas, P., Flecher, E., Fest, T., Tarte, K., 2015. Neutrophils trigger a NF-κB dependent polarization of tumor-supportive stromal cells in germinal center B-cell lymphomas. Oncotarget 6, 16471–16487. doi:10.18632/oncotarget.4106

Guilloton, F., Caron, G., Ménard, C., Pangault, C., Amé-Thomas, P., Dulong, J., De Vos, J., Rossille, D., Henry, C., Lamy, T., Fouquet, O., Fest, T., Tarte, K., 2012. Mesenchymal stromal cells orchestrate follicular lymphoma cell niche through the CCL2-dependent recruitment and polarization of monocytes. Blood 119, 2556–2567. doi:10.1182/blood-2011-08-370908

Heesters, B.A., Myers, R.C., Carroll, M.C., 2014. Follicular dendritic cells: dynamic antigen libraries. Nat. Rev. Immunol. 14, 495–504. doi:10.1038/nri3689

Heinig, K., Gätjen, M., Grau, M., Stache, V., Anagnostopoulos, I., Gerlach, K., Niesner, R.A., Cseresnyes, Z., Hauser, A.E., Lenz, P., Hehlgans, T., Brink, R., Westermann, J., Dörken, B., Lipp, M., Lenz, G., Rehm, A., Höpken, U.E., 2014. Access to follicular dendritic cells is a pivotal step in murine chronic lymphocytic leukemia B-cell activation and proliferation. Cancer Discov 4, 1448–1465. doi:10.1158/2159-8290.CD-14-0096

Huang, H.-Y., Rivas-Caicedo, A., Renevey, F., Cannelle, H., Peranzoni, E., Scarpellino, L., Hardie, D.L., Pommier, A., Schaeuble, K., Favre, S., Vogt, T.K., Arenzana-Seisdedos, F., Schneider, P., Buckley, C.D., Donnadieu, E., Luther, S.A., 2018. Identification of a new subset of lymph node stromal cells involved in regulating plasma cell homeostasis. Proc. Natl. Acad. Sci. U.S.A. 115, E6826–E6835. doi:10.1073/pnas.1712628115

Huet, S., Sujobert, P., Salles, G., 2018a. From genetics to the clinic: a translational perspective on follicular lymphoma. Nat. Rev. Cancer 18, 224–239. doi:10.1038/nrc.2017.127

Huet, S., Tesson, B., Jais, J.-P., Feldman, A.L., Magnano, L., Thomas, E., Traverse-Glehen, A., Albaud, B., Carrère, M., Xerri, L., Ansell, S.M., Baseggio, L., Reyes, C., Tarte, K., Boyault, S., Haioun, C., Link, B.K., Feugier, P., Lopez-Guillermo, A., Tilly, H., Brice, P., Hayette, S., Jardin, F., Offner, F., Sujobert, P., Gentien, D., Viari, A., Campo, E., Cerhan, J.R., Salles, G., 2018b. A gene-expression profiling score

for prediction of outcome in patients with follicular lymphoma: a retrospective training and validation analysis in three international cohorts. Lancet Oncol 19, 549–561. doi:10.1016/S1470-2045(18)30102-5

Jarjour, M., Jorquera, A., Mondor, I., Wienert, S., Narang, P., Coles, M.C., Klauschen, F., Bajénoff, M., 2014. Fate mapping reveals origin and dynamics of lymph node follicular dendritic cells. J. Exp. Med. 211, 1109–1122. doi:10.1084/jem.20132409

Kim, Jini, Lee, S., Kim, Y.-M., Jeoung, D.-I., Choe, J., 2013. Human follicular dendritic cells promote germinal center B cell survival by providing prostaglandins. Mol. Immunol. 55, 418–423. doi:10.1016/j.molimm.2013.03.019

Kim, Jungtae, Kim, D.W., Chang, W., Choe, J., Kim, J., Park, C.-S., Song, K., Lee, I., 2012. Wnt5a is secreted by follicular dendritic cells to protect germinal center B cells via Wnt/Ca2+/NFAT/NF-κB-B cell lymphoma 6 signaling. J. Immunol. 188, 182–189. doi:10.4049/jimmunol.1102297

Knoblich, K., Cruz Migoni, S., Siew, S.M., Jinks, E., Kaul, B., Jeffery, H.C., Baker, A.T., Suliman, M., Vrzalikova, K., Mehenna, H., Murray, P.G., Barone, F., Oo, Y.H., Newsome, P.N., Hirschfield, G., Kelly, D., Lee, S.P., Parekkadan, B., Turley, S.J., Fletcher, A.L., 2018. The human lymph node microenvironment unilaterally regulates T-cell activation and differentiation. PLoS Biol. 16, e2005046. doi:10.1371/journal.pbio.2005046

Krautler, N.J., Kana, V., Kranich, J., Tian, Y., Perera, D., Lemm, D., Schwarz, P., Armulik, A., Browning, J.L., Tallquist, M., Buch, T., Oliveira-Martins, J.B., Zhu, C., Hermann, M., Wagner, U., Brink, R., Heikenwalder, M., Aguzzi, A., 2012. Follicular dendritic cells emerge from ubiquitous perivascular precursors. Cell 150, 194–206. doi:10.1016/j.cell.2012.05.032

Krishnamurty, A.T., Turley, S.J., 2020. Lymph node stromal cells: cartographers of the immune system. Nat. Immunol. 21, 369–380. doi:10.1038/s41590-020-0635-3

Lamaison, C., Tarte, K., 2019. Impact of B cell/lymphoid stromal cell crosstalk in B-cell physiology and malignancy. Immunol. Lett. 215, 12–18. doi:10.1016/j.imlet.2019.02.005

Langfelder, P., Horvath, S., 2008. WGCNA: an R package for weighted correlation network analysis. BMC Bioinformatics 9, 559. doi:10.1186/1471-2105-9-559

Li, H., Ghazanfari, R., Zacharaki, D., Ditzel, N., Isern, J., Ekblom, M., Méndez-Ferrer, S., Kassem, M., Scheding, S., 2014. Low/negative expression of PDGFR-α identifies the candidate primary mesenchymal stromal cells in adult human bone marrow. Stem Cell Reports 3, 965–974. doi:10.1016/j.stemcr.2014.09.018

Liao, Y., Smyth, G.K., Shi, W., 2014. featureCounts: an efficient general purpose program for assigning sequence reads to genomic features. Bioinformatics 30, 923–930. doi:10.1093/bioinformatics/btt656

Link, A., Vogt, T.K., Favre, S., Britschgi, M.R., Acha-Orbea, H., Hinz, B., Cyster, J.G., Luther, S.A., 2007. Fibroblastic reticular cells in lymph nodes regulate the homeostasis of naive T cells. Nat. Immunol. 8, 1255–1265. doi:10.1038/ni1513

Liu, Y.J., Xu, J., de Bouteiller, O., Parham, C.L., Grouard, G., Djossou, O., de Saint-Vis, B., Lebecque, S., Banchereau, J., Moore, K.W., 1997. Follicular dendritic cells specifically express the long CR2/CD21 isoform. J. Exp. Med. 185, 165–170. doi:10.1084/jem.185.1.165

Lu, E., Cyster, J.G., 2019. G-protein coupled receptors and ligands that organize humoral immune responses. Immunol. Rev. 289, 158–172. doi:10.1111/imr.12743

Malhotra, D., Fletcher, A.L., Astarita, J., Lukacs-Kornek, V., Tayalia, P., Gonzalez, S.F., Elpek, K.G., Chang, S.K., Knoblich, K., Hemler, M.E., Brenner, M.B., Carroll, M.C., Mooney, D.J., Turley, S.J., Immunological Genome Project Consortium,

2012. Transcriptional profiling of stroma from inflamed and resting lymph nodes defines immunological hallmarks. Nat. Immunol. 13, 499–510. doi:10.1038/ni.2262

Ménard, C., Dulong, J., Roulois, D., Hébraud, B., Verdière, L., Pangault, C., Sibut, V., Bezier, I., Bescher, N., Monvoisin, C., Gadelorge, M., Bertheuil, N., Flecher, E., Casteilla, L., Collas, P., Sensebé, L., Bourin, P., Espagnolle, N., Tarte, K., 2019. Integrated Transcriptomic, Phenotypic, and Functional Study Reveals Tissue-Specific Immune Properties of Mesenchymal Stromal Cells. Stem Cells 14, 493. doi:10.1002/stem.3077

Middendorp, S., Xiao, Y., Song, J.-Y., Peperzak, V., Krijger, P.H.L., Jacobs, H., Borst, J., 2009. Mice deficient for CD137 ligand are predisposed to develop germinal center-derived B-cell lymphoma. Blood 114, 2280–2289. doi:10.1182/blood-2009-03-208215

Mueller, S.N., Germain, R.N., 2009. Stromal cell contributions to the homeostasis and functionality of the immune system. Nat. Rev. Immunol. 9, 618–629. doi:10.1038/nri2588

Munoz, O., Fend, F., de Beaumont, R., Husson, H., Astier, A., Freedman, A.S., 2004. TGFbeta-mediated activation of Smad1 in B-cell non-Hodgkin's lymphoma and effect on cell proliferation. Leukemia 18, 2015–2025. doi:10.1038/sj.leu.2403485

Muppidi, J.R., Schmitz, R., Green, J.A., Xiao, W., Larsen, A.B., Braun, S.E., An, J., Xu, Y., Rosenwald, A., Ott, G., Gascoyne, R.D., Rimsza, L.M., Campo, E., Jaffe, E.S., Delabie, J., Smeland, E.B., Braziel, R.M., Tubbs, R.R., Cook, J.R., Weisenburger, D.D., Chan, W.C., Vaidehi, N., Staudt, L.M., Cyster, J.G., 2014. Loss of signalling via Gα13 in germinal centre B-cell-derived lymphoma. Nature 516, 254–258. doi:10.1038/nature13765

O'Donnell, J.S., Madore, J., Li, X.-Y., Smyth, M.J., 2019. Tumor intrinsic and extrinsic immune functions of CD155. Semin. Cancer Biol. doi:10.1016/j.semcancer.2019.11.013

Ortega-Molina, A., Deleyto-Seldas, N., Carreras, J., Sanz, A., Lebrero-Fernández, C., Menéndez, C., Vandenberg, A., Fernández-Ruiz, B., Marín-Arraiza, L., la Calle Arregui, de, C., Belén Plata-Gómez, A., Caleiras, E., de Martino, A., Martínez-Martín, N., Troulé, K., Piñeiro-Yáñez, E., Nakamura, N., Araf, S., Victora, G.D., Okosun, J., Fitzgibbon, J., Efeyan, A., 2019. Oncogenic Rag GTPase signaling enhances B cell activation and drives follicular lymphoma sensitive to pharmacological inhibition of mTOR. Nat Metab 1, 775–789. doi:10.1038/s42255-019-0098-8

Pandey, S., Mourcin, F., Marchand, T., Nayar, S., Guirriec, M., Pangault, C., Monvoisin, C., Amé-Thomas, P., Guilloton, F., Dulong, J., Coles, M., Fest, T., Mottok, A., Barone, F., Tarte, K., 2017. IL-4/CXCL12 loop is a key regulator of lymphoid stroma function in follicular lymphoma. Blood 129, 2507–2518. doi:10.1182/blood-2016-08-737239

Pangault, C., Amé-Thomas, P., Rossille, D., Dulong, J., Caron, G., Nonn, C., Chatonnet, F., Desmots, F., Launay, V., Lamy, T., Fest, T., Tarte, K., 2020. Integrative Analysis of Cell Crosstalk within Follicular Lymphoma Cell Niche: Towards a Definition of the FL Supportive Synapse. Cancers (Basel) 12. doi:10.3390/cancers12102865

Pangault, C., Amé-Thomas, P., Ruminy, P., Rossille, D., Caron, G., Baia, M., De Vos, J., Roussel, M., Monvoisin, C., Lamy, T., Tilly, H., Gaulard, P., Tarte, K., Fest, T., 2010. Follicular lymphoma cell niche: identification of a preeminent IL-4-dependent T(FH)-B cell axis. Leukemia 24, 2080–2089. doi:10.1038/leu.2010.223

Park, E., Chen, J., Moore, A., Mangolini, M., Santoro, A., Boyd, J.R., Schjerven, H.,

Ecker, V., Buchner, M., Williamson, J.C., Lehner, P.J., Gasparoli, L., Williams, O., Bloehdorn, J., Stilgenbauer, S., Leitges, M., Egle, A., Schmidt-Supprian, M., Frietze, S., Ringshausen, I., 2020. Stromal cell protein kinase C-β inhibition enhances chemosensitivity in B cell malignancies and overcomes drug resistance. Sci Transl Med 12, eaax9340. doi:10.1126/scitranslmed.aax9340

Pepe, G., Di Napoli, A., Cippitelli, C., Scarpino, S., Pilozzi, E., Ruco, L., 2018. Reduced lymphotoxin-beta production by tumour cells is associated with loss of follicular dendritic cell phenotype and diffuse growth in follicular lymphoma. J Pathol Clin Res 4, 124–134. doi:10.1002/cjp2.97

Perez-Shibayama, C., Gil-Cruz, C., Ludewig, B., 2019. Fibroblastic reticular cells at the nexus of innate and adaptive immune responses. Immunol. Rev. 289, 31–41. doi:10.1111/imr.12748

Pikor, N.B., Mörbe, U., Lütge, M., Gil-Cruz, C., Perez-Shibayama, C., Novkovic, M., Cheng, H.-W., Nombela-Arrieta, C., Nagasawa, T., Linterman, M.A., Onder, L., Ludewig, B., 2020. Remodeling of light and dark zone follicular dendritic cells governs germinal center responses. Nat. Immunol. 21, 649–659. doi:10.1038/s41590-020-0672-y

Riedel, A., Shorthouse, D., Haas, L., Hall, B.A., Shields, J., 2016. Tumor-induced stromal reprogramming drives lymph node transformation. Nat. Immunol. 17, 1118–1127. doi:10.1038/ni.3492

Rodda, L.B., Lu, E., Bennett, M.L., Sokol, C.L., Wang, X., Luther, S.A., Barres, B.A., Luster, A.D., Ye, C.J., Cyster, J.G., 2018. Single-Cell RNA Sequencing of Lymph Node Stromal Cells Reveals Niche-Associated Heterogeneity. Immunity 48, 1014–1028.e6. doi:10.1016/j.immuni.2018.04.006

Sacchetti, B., Funari, A., Michienzi, S., Di Cesare, S., Piersanti, S., Saggio, I., Tagliafico, E., Ferrari, S., Robey, P.G., Riminucci, M., Bianco, P., 2007. Self-renewing osteoprogenitors in bone marrow sinusoids can organize a hematopoietic microenvironment. Cell 131, 324–336. doi:10.1016/j.cell.2007.08.025

Sacchetti, B., Funari, A., Remoli, C., Giannicola, G., Kögler, G., Liedtke, S., Cossu, G., Serafini, M., Sampaolesi, M., Tagliafico, E., Tenedini, E., Saggio, I., Robey, P.G., Riminucci, M., Bianco, P., 2016. No Identical "Mesenchymal Stem Cells" at Different Times and Sites: Human Committed Progenitors of Distinct Origin and Differentiation Potential Are Incorporated as Adventitial Cells in Microvessels. Stem Cell Reports 6, 897–913. doi:10.1016/j.stemcr.2016.05.011

Sahai, E., Astsaturov, I., Cukierman, E., DeNardo, D.G., Egeblad, M., Evans, R.M., Fearon, D., Greten, F.R., Hingorani, S.R., Hunter, T., Hynes, R.O., Jain, R.K., Janowitz, T., Jorgensen, C., Kimmelman, A.C., Kolonin, M.G., Maki, R.G., Powers, R.S., Puré, E., Ramirez, D.C., Scherz-Shouval, R., Sherman, M.H., Stewart, S., Tlsty, T.D., Tuveson, D.A., Watt, F.M., Weaver, V., Weeraratna, A.T., Werb, Z., 2020. A framework for advancing our understanding of cancer-associated fibroblasts. Nat. Rev. Cancer 20, 174–186. doi:10.1038/s41568-019-0238-1

Salmon, H., Franciszkiewicz, K., Damotte, D., Dieu-Nosjean, M.-C., Validire, P., Trautmann, A., Mami-Chouaib, F., Donnadieu, E., 2012. Matrix architecture defines the preferential localization and migration of T cells into the stroma of human lung tumors. J. Clin. Invest. 122, 899–910. doi:10.1172/JCI45817

Severino, P., Palomino, D.T., Alvarenga, H., Almeida, C.B., Pasqualim, D.C., Cury, A., Salvalaggio, P.R., De Vasconcelos Macedo, A.L., Andrade, M.C., Aloia, T., Bromberg, S., Rizzo, L.V., Rocha, F.A., Marti, L.C., 2017. Human Lymph Node-Derived Fibroblastic and Double-Negative Reticular Cells Alter Their Chemokines

and Cytokines Expression Profile Following Inflammatory Stimuli. Front Immunol 8, 141. doi:10.3389/fimmu.2017.00141

Shibuya, A., Honda, S.-I., 2015. Immune regulation by Fcα/μ receptor (CD351) on marginal zone B cells and follicular dendritic cells. Immunol. Rev. 268, 288–295. doi:10.1111/imr.12345

Sitnik, K.M., Wendland, K., Weishaupt, H., Uronen-Hansson, H., White, A.J., Anderson, G., Kotarsky, K., Agace, W.W., 2016. Context-Dependent Development of Lymphoid Stroma from Adult CD34(+) Adventitial Progenitors. Cell Rep 14, 2375–2388. doi:10.1016/j.celrep.2016.02.033

Stuart, T., Butler, A., Hoffman, P., Hafemeister, C., Papalexi, E., Mauck, W.M., Hao, Y., Stoeckius, M., Smibert, P., Satija, R., 2019. Comprehensive Integration of Single-Cell Data. Cell 177, 1888–1902.e21. doi:10.1016/j.cell.2019.05.031

Suzuki, K., Maruya, M., Kawamoto, S., Sitnik, K., Kitamura, H., Agace, W.W., Fagarasan, S., 2010. The sensing of environmental stimuli by follicular dendritic cells promotes immunoglobulin A generation in the gut. Immunity 33, 71–83. doi:10.1016/j.immuni.2010.07.003

Takeuchi, A., Ozawa, M., Kanda, Y., Kozai, M., Ohigashi, I., Kurosawa, Y., Rahman, M.A., Kawamura, T., Shichida, Y., Umemoto, E., Miyasaka, M., Ludewig, B., Takahama, Y., Nagasawa, T., Katakai, T., 2018. A Distinct Subset of Fibroblastic Stromal Cells Constitutes the Cortex-Medulla Boundary Subcompartment of the Lymph Node. Front Immunol 9, 2196. doi:10.3389/fimmu.2018.02196

Thomazy, V.A., Vega, F., Medeiros, L.J., Davies, P.J., Jones, D., 2003. Phenotypic modulation of the stromal reticular network in normal and neoplastic lymph nodes: tissue transglutaminase reveals coordinate regulation of multiple cell types. Am. J. Pathol. 163, 165–174. doi:10.1016/S0002-9440(10)63640-1

Yang, C.-Y., Vogt, T.K., Favre, S., Scarpellino, L., Huang, H.-Y., Tacchini-Cottier, F., Luther, S.A., 2014. Trapping of naive lymphocytes triggers rapid growth and remodeling of the fibroblast network in reactive murine lymph nodes. Proc. Natl. Acad. Sci. U.S.A. 111, E109–18. doi:10.1073/pnas.1312585111

Yang, Z.-Z., Grote, D.M., Xiu, B., Ziesmer, S.C., Price-Troska, T.L., Hodge, L.S., Yates, D.M., Novak, A.J., Ansell, S.M., 2014. TGF-β upregulates CD70 expression and induces exhaustion of effector memory T cells in B-cell non-Hodgkin's lymphoma. Leukemia 28, 1872–1884. doi:10.1038/leu.2014.84

Yang, Z.-Z., Grote, D.M., Ziesmer, S.C., Xiu, B., Yates, N.R., Secreto, F.J., Hodge, L.S., Witzig, T.E., Novak, A.J., Ansell, S.M., 2013. Soluble and membrane-bound TGF-β-mediated regulation of intratumoral T cell differentiation and function in B-cell non-Hodgkin lymphoma. PLoS ONE 8, e59456. doi:10.1371/journal.pone.0059456

Yoon, S.-O., Zhang, X., Berner, P., Blom, B., Choi, Y.S., 2009. Notch ligands expressed by follicular dendritic cells protect germinal center B cells from apoptosis. J. Immunol. 183, 352–358. doi:10.4049/jimmunol.0803183

Zhang, Y., Tech, L., George, L.A., Acs, A., Durrett, R.E., Hess, H., Walker, L.S.K., Tarlinton, D.M., Fletcher, A.L., Hauser, A.E., Toellner, K.-M., 2018. Plasma cell output from germinal centers is regulated by signals from Tfh and stromal cells. J. Exp. Med. 215, 1227–1243. doi:10.1084/jem.20160832

Wu, X., Xiao, Y., Zhou, Y., Yan, W., 2019, LncRNA FOXP4-AS1 is activated by PAX5 and promotes the growth of prostate cancer by sequestering miR-3184-5p to upregulate FOXP4. Cell Death Dis. 10, 472. doi: 10.1038/s41419-1699-6.

Figure 1. Human LSC subset identification

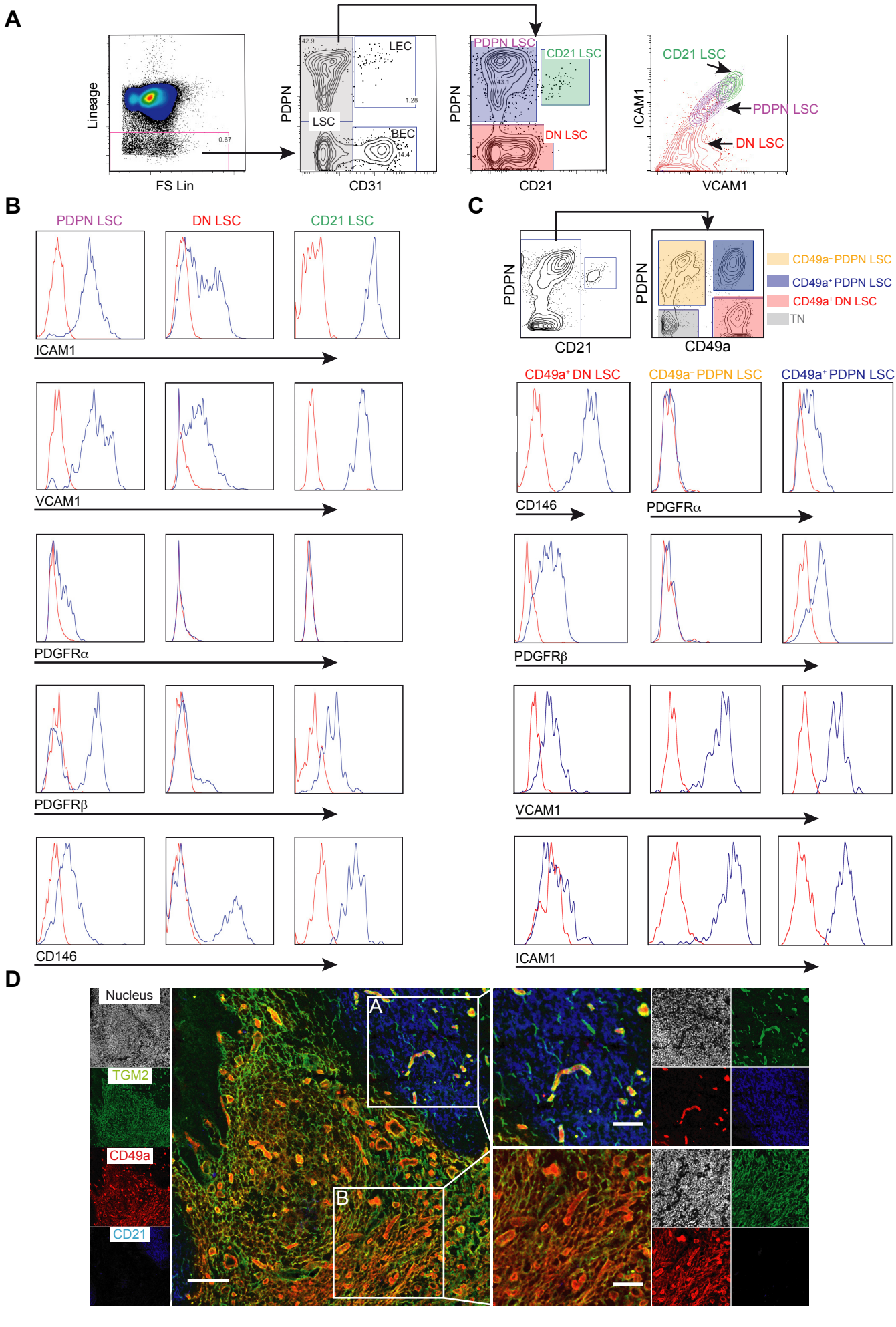

Figure 2. Transcriptomic characterization of human LSC subsets

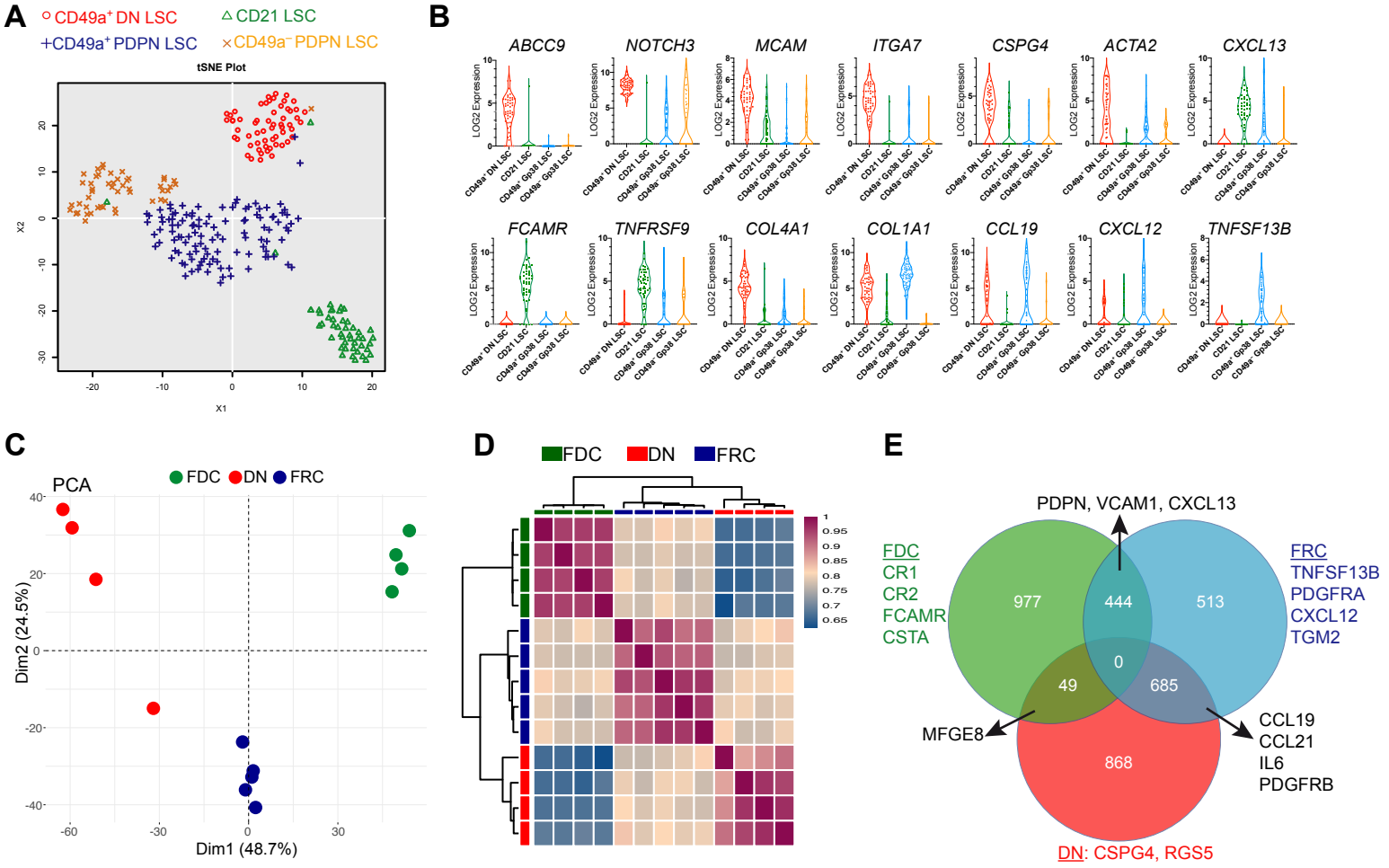

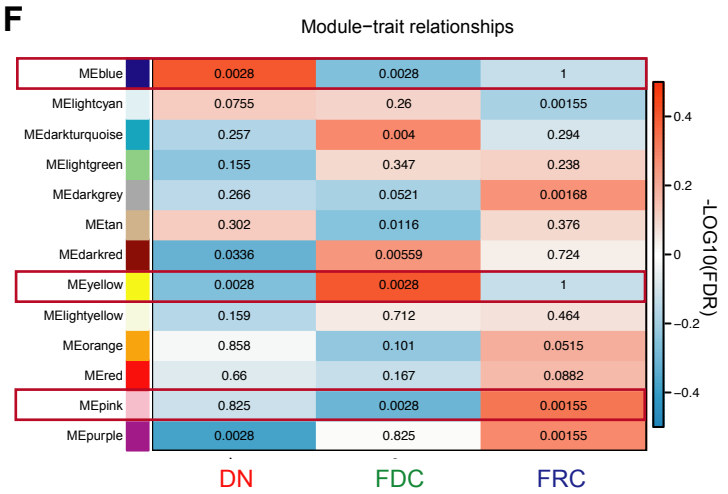

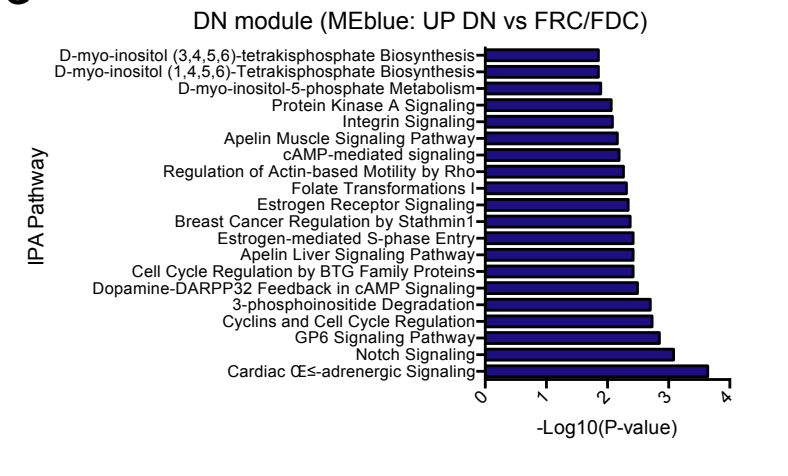

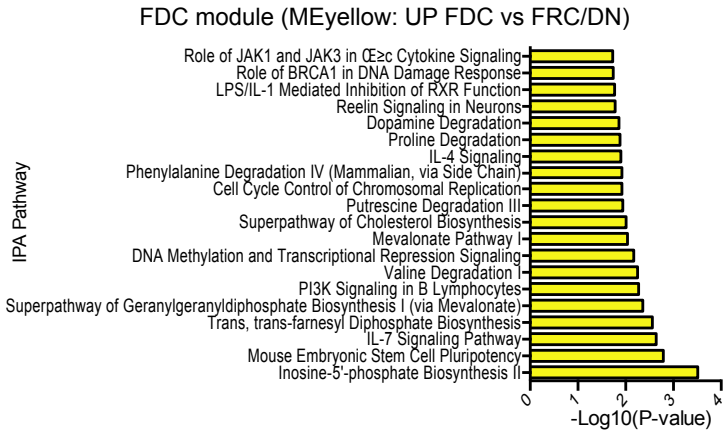

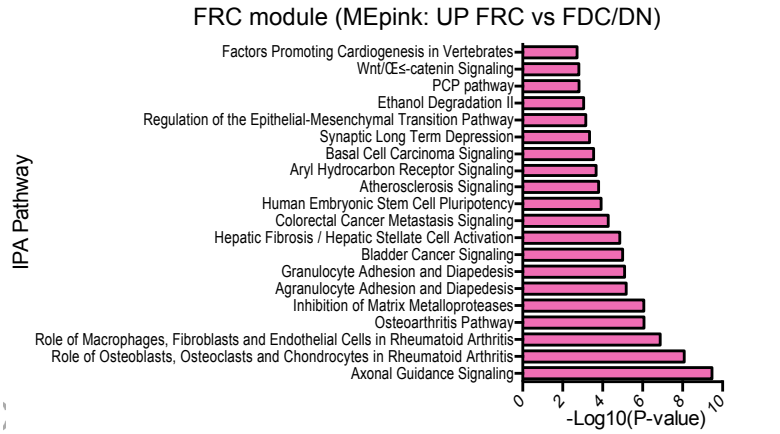

Figure 3. Characterization of human DNs

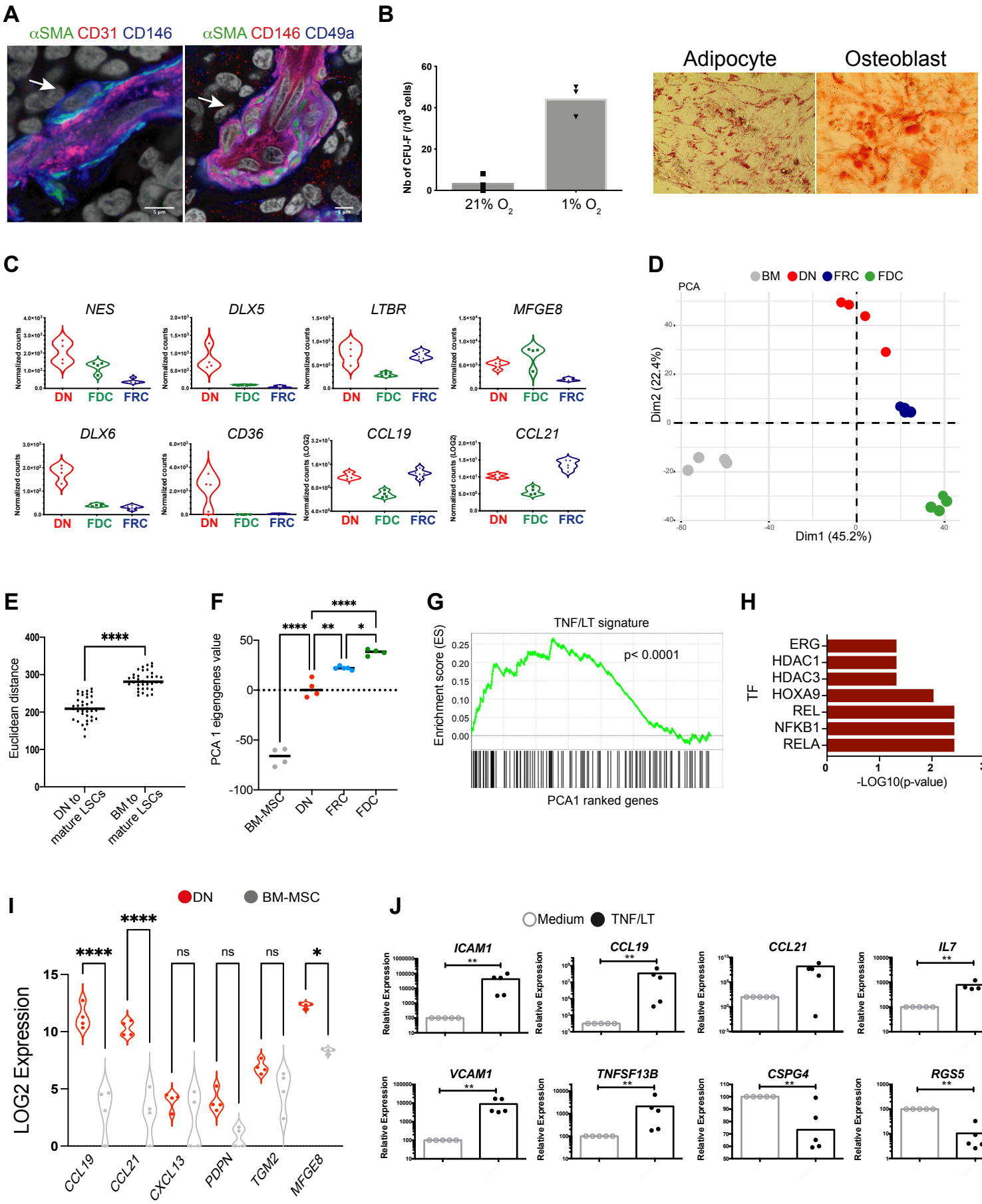

Figure 4. Characterization of human FRCs

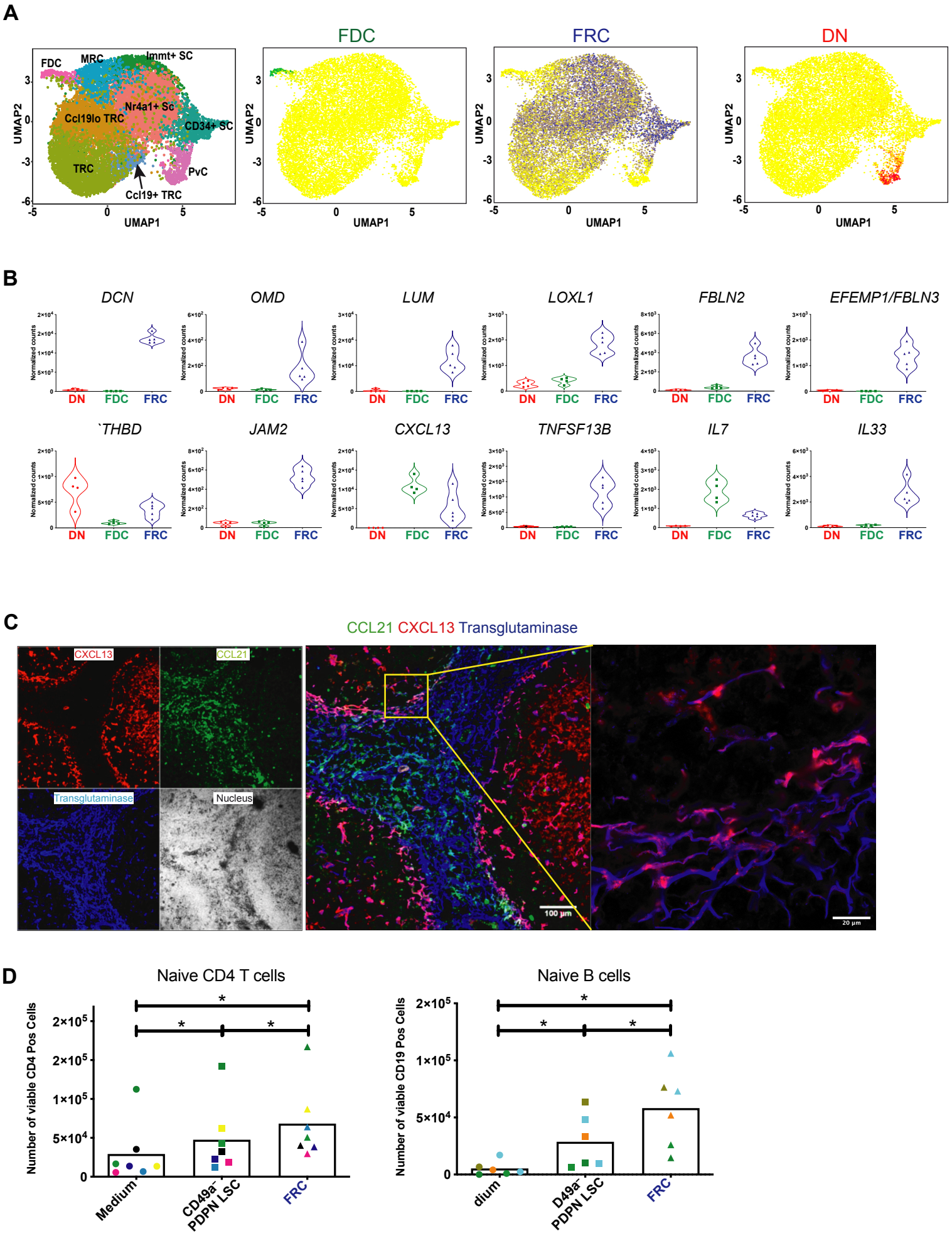

Figure 5. Characterization of human FDCs

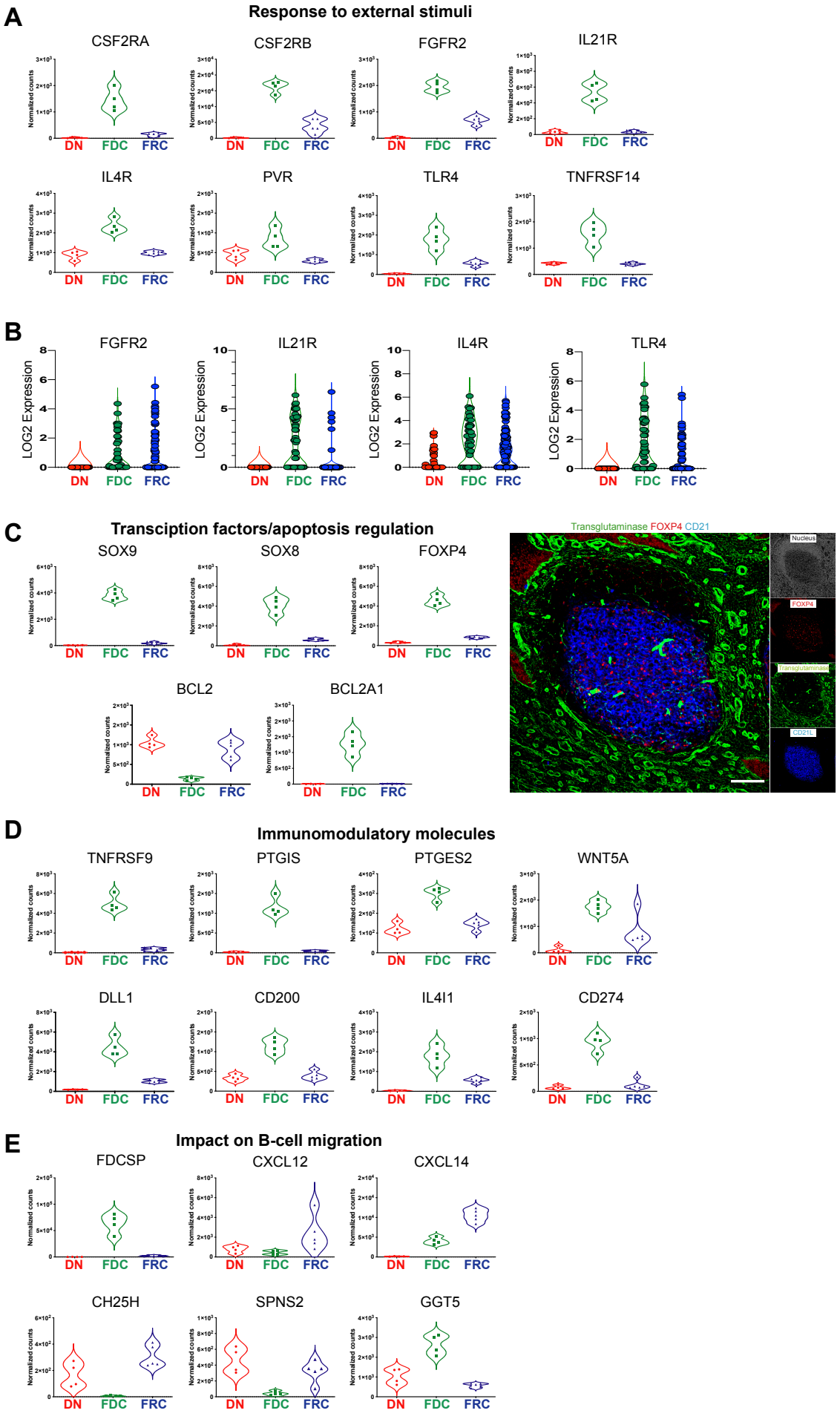

Figure 6. Interactions between FL B cells and LSCs

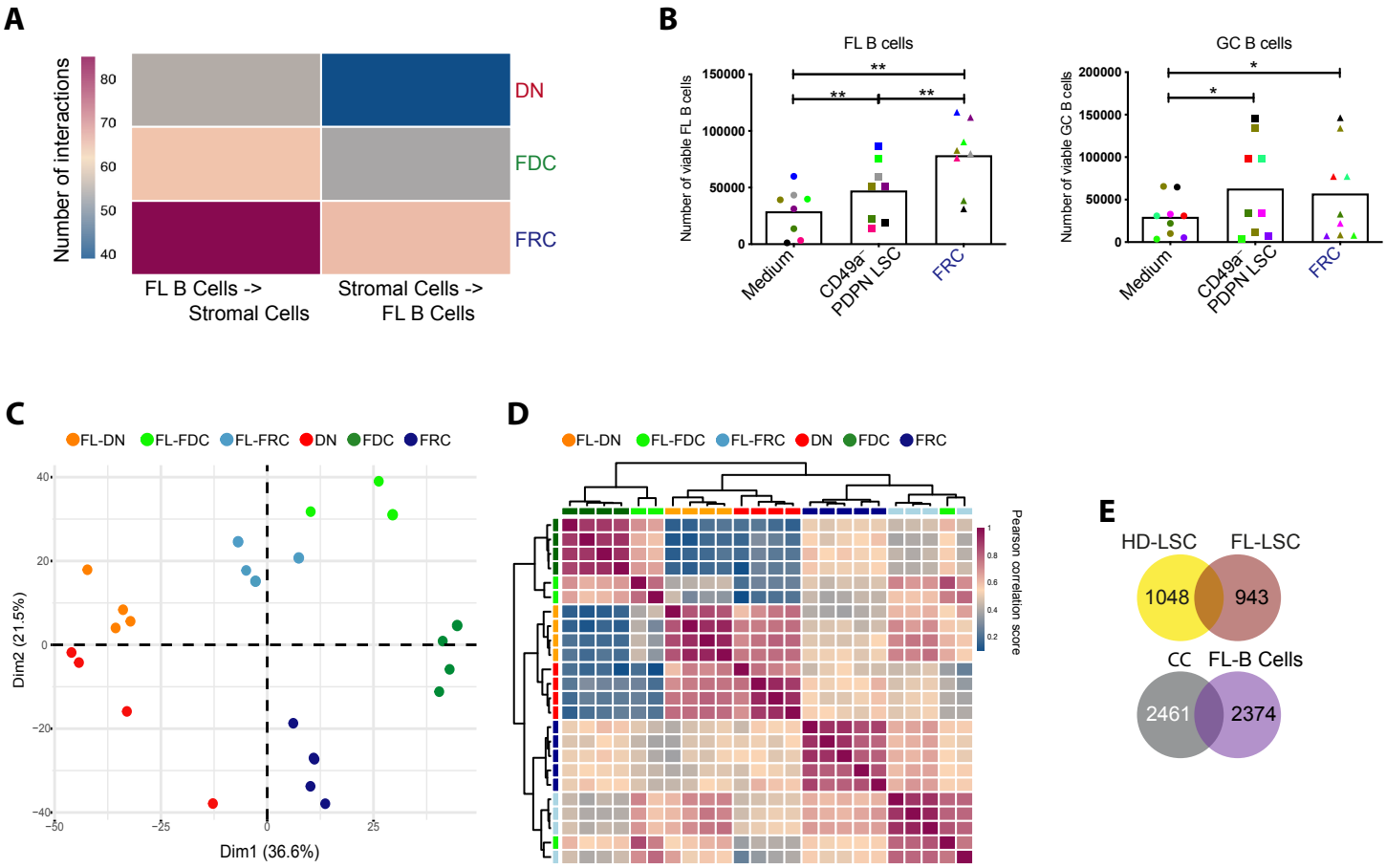

Figure 7. FL-LSC commitment in situ

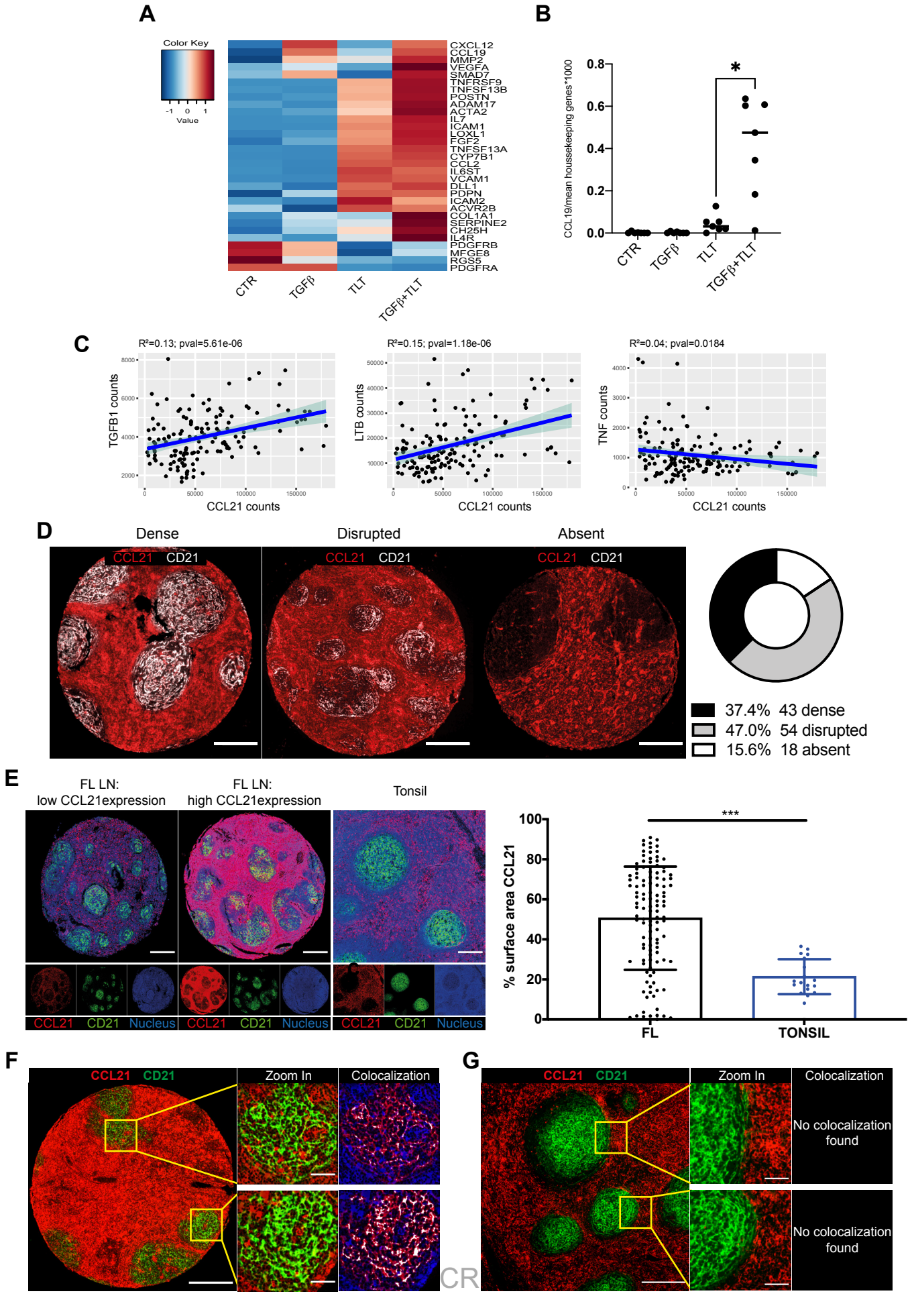

Supplemental Figure 1. *In situ* and *ex vivo* characterization of human LSCs (related to Figure 1).

A) Architecture of a tonsil section obtained by immunofluorescence after staining for B cells (CD79a, Green), PDPN (Red), and CD21 (Blue). Nuclei were counterstained with SytoxBlue (White). Scale bars, 100µm.

B) Comparison between tonsil and lymph node LSC organization was performed by immunofluorescence for B cells (CD20, Red), TGM2/Transglutaminase (Green), and CD21 (Blue). Nuclei were counterstained with SytoxBlue (White). Scale bars, 200µm.

C) Expression of adhesion molecules on tonsil sections. Left: TGM2/Transglutaminase (Green), VCAM1 (Red), and Nucleus (White). Right: TGM2/Transglutaminase (Green), ICAM1 (Red), and Nucleus (White). Scale bars, 200µm.

D) Expression of lymphoid stroma markers (*TGM2*, *PDPN*, and *CD21*) was studied by Q-PCR on sorted LSC subsets including DN LSCs (n=3), CD21 LSCs (n=3), and PDPN LSCs (n=3). Data represent the relative expression of corresponding genes as compared to a pool of tonsil cells.

E) Comparison of the CD49a expression on the different LSC subsets by flow cytometry.

F) Analysis of the percentage of $PDPN^{-}$ $CD49a^{-}$ $CD21^{-}$ triple negative stromal cells (TN) by flow cytometry. The percentage of TNs within $CD21^{-}$ LSC was first evaluated before depletion of $CD45^{+}$ hematopoietic cells with non-restrictive (gating strategy # 1) or restrictive (gating strategy # 2) gating strategies to define $Lineage^{-}$ stromal cells. TN percentage was also evaluated after previous depletion of $CD45^{+}$ hematopoietic cells (third line).

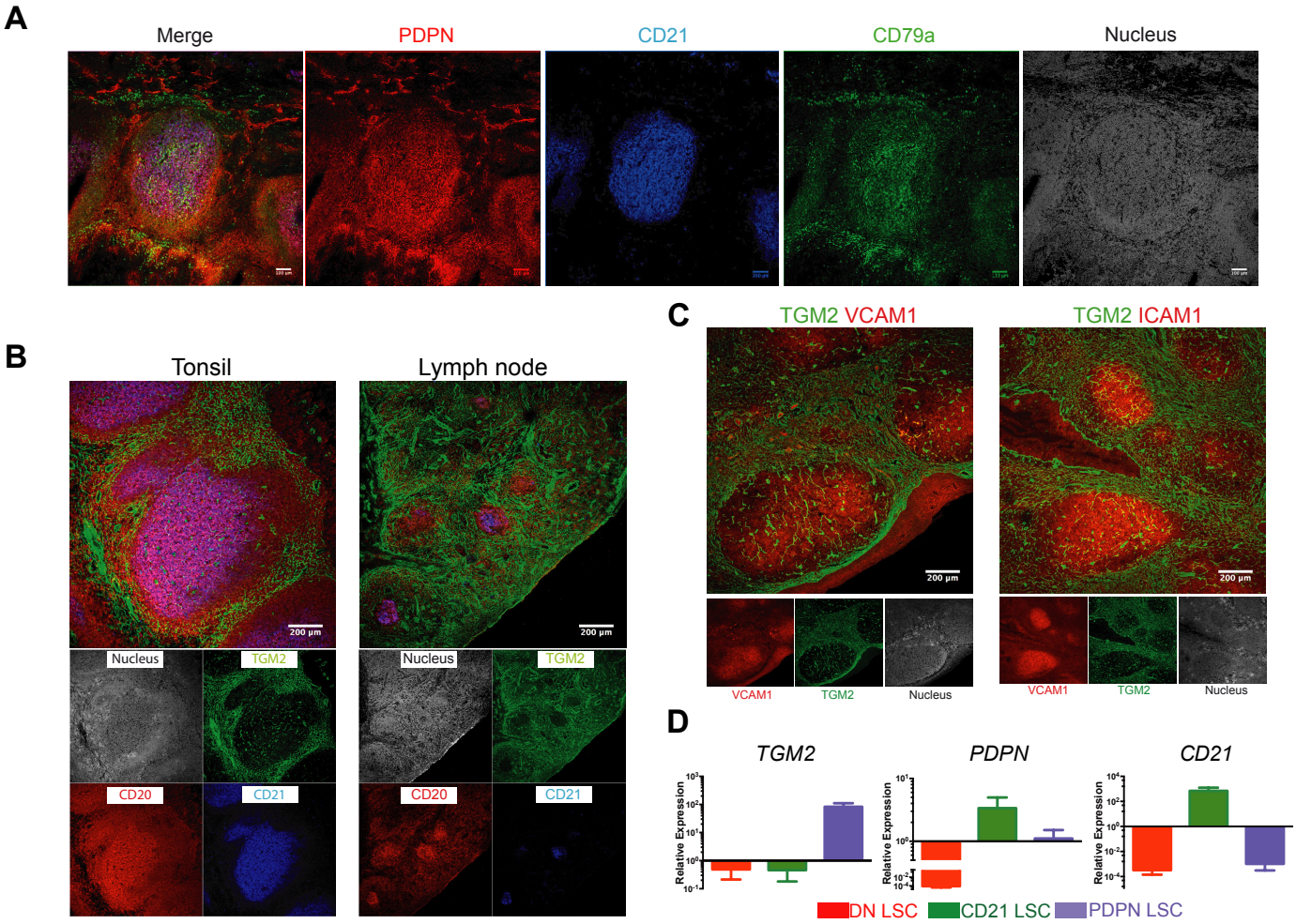
A
Merge
PDPN
CD21
CD79a
Nucleus
B
Tonsil
Lymph node
Nucleus
TGM2
CD20
CD21
200 µm
C
TGM2 VCAM1
TGM2 ICAM1
VCAM1
TGM2
Nucleus
D
TGM2
PDPN
CD21
Relative Expression
DN LSC
CD21 LSC
PDPN LSC
E
Lineage
FSC-A
CD21
CD49a
F
Gating strategy #1
Gating strategy #2
Before CD45 depletion
After CD45 depletion
0.36
98.5
1.20
33.2
0.18
98.8
1.06
12.0
47.3
88.4
10.8
2.56
PDPN

Supplemental Figure 2: Transcriptomic characterization of human LSC subsets (related to Figure 2).

A) Heat maps of LSC subset gene expression. Shown is the Log2-normalized expression scaled for each gene.

B) The comparison between human and mouse LSC transcriptomes was performed by GSEA. Affymetrix gene expression profiles of FRCs and DNs from mouse skin lymph nodes were obtained from Immunological Genome Project Consortium (Malhotra et al., 2012). The graphs show the enrichment plots generated by GSEA of ranked gene expression data for the specific murine gene signatures. The gene expression data were preranked based on the wald test used to compare the human (h) samples (hFRC vs hDN and hFDC vs hDN).

C) WGCNA analysis of human LSC subsets. The soft-thresholding power was selected (upper panels) based on the evolution of the scale free topology index in function of the soft threshold (left) and the analysis of the mean connectivity evolution in function of the soft threshold (right). Lower panel shows the gene clustering dendrogram and module delimitation based on topological overlap, with different colors representing different co-expression gene modules.

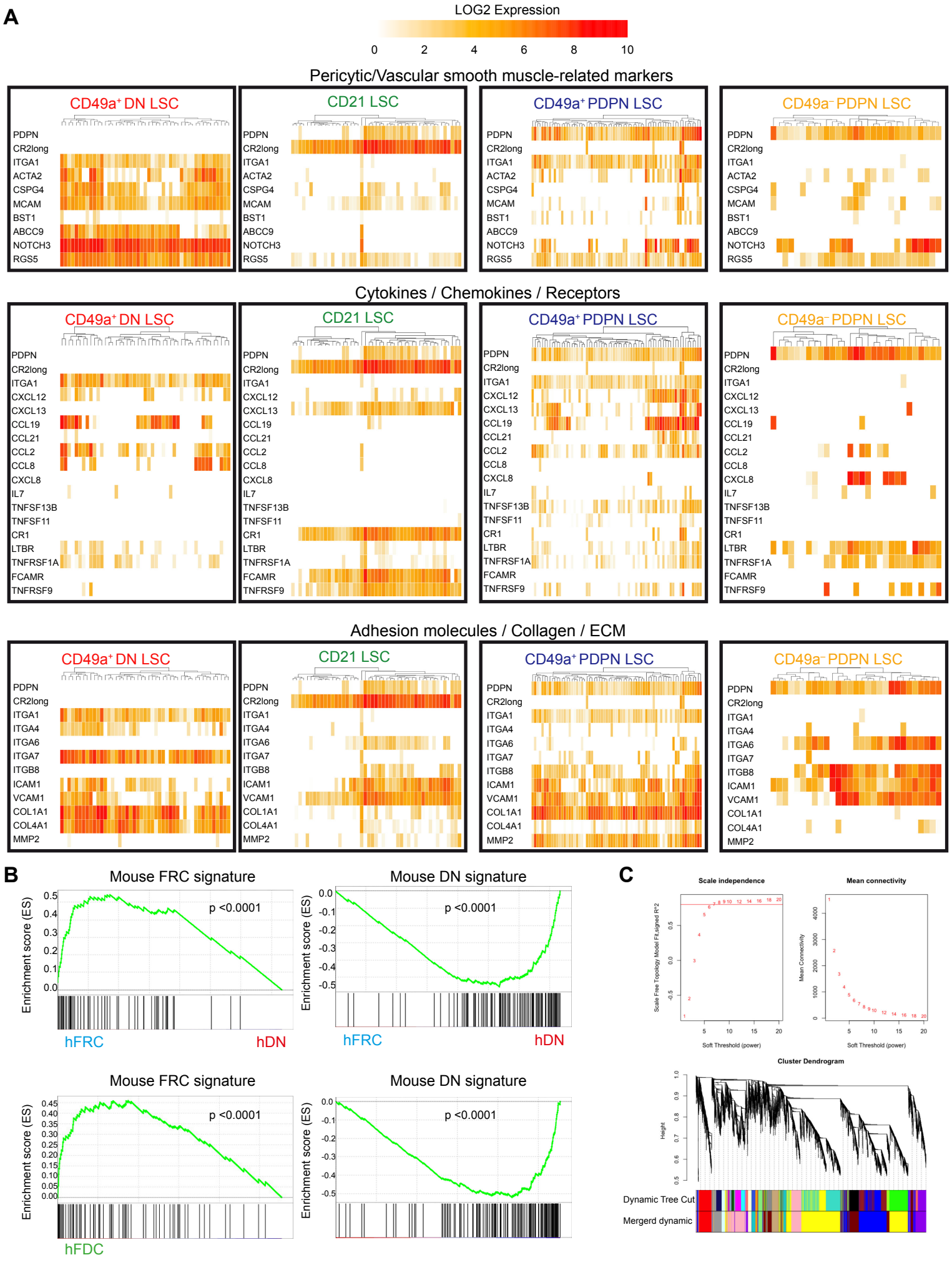
A
LOG2 Expression
0
2
4
6
8
10
Pericytic/Vascular smooth muscle-related markers
CD49a+ DN LSC
CD21 LSC
CD49a+ PDPN LSC
CD49a− PDPN LSC
PDPN
CR2long
ITGA1
ACTA2
CSPG4
MCAM
BST1
ABCC9
NOTCH3
RGS5
Cytokines / Chemokines / Receptors
CXCL12
CXCL13
CCL19
CCL21
CCL2
CCL8
CXCL8
IL7
TNFSF13B
TNFSF11
CR1
LTBR
TNFRSF1A
FCAMR
TNFRSF9
Adhesion molecules / Collagen / ECM
ITGA4
ITGA6
ITGA7
ITGB8
ICAM1
VCAM1
COL1A1
COL4A1
MMP2
B
Mouse FRC signature
Mouse DN signature
Enrichment score (ES)
p <0.0001
hFRC
hDN
hFDC
C
Scale independence
Mean connectivity
Scale Free Topology Model Fit,signed R^2
Mean Connectivity
Soft Threshold (power)
Cluster Dendrogram
Height
Dynamic Tree Cut
Mergerd dynamic

Supplemental Figure 3. Expression of immunologically relevant ligands and receptors by human LSCs (related to Figure 2).

Heat-map analysis of the expression of cytokines/cytokine receptors, growth factors/growth factor receptors, adhesion molecules, extracellular matrix components as evaluated by RNA-seq from cell-sorted DNs (n=4), FDCs (n=4), and FRCs (n=5). Shown is the mean value of log2-transformed normalized data. Green indicated higher expression.

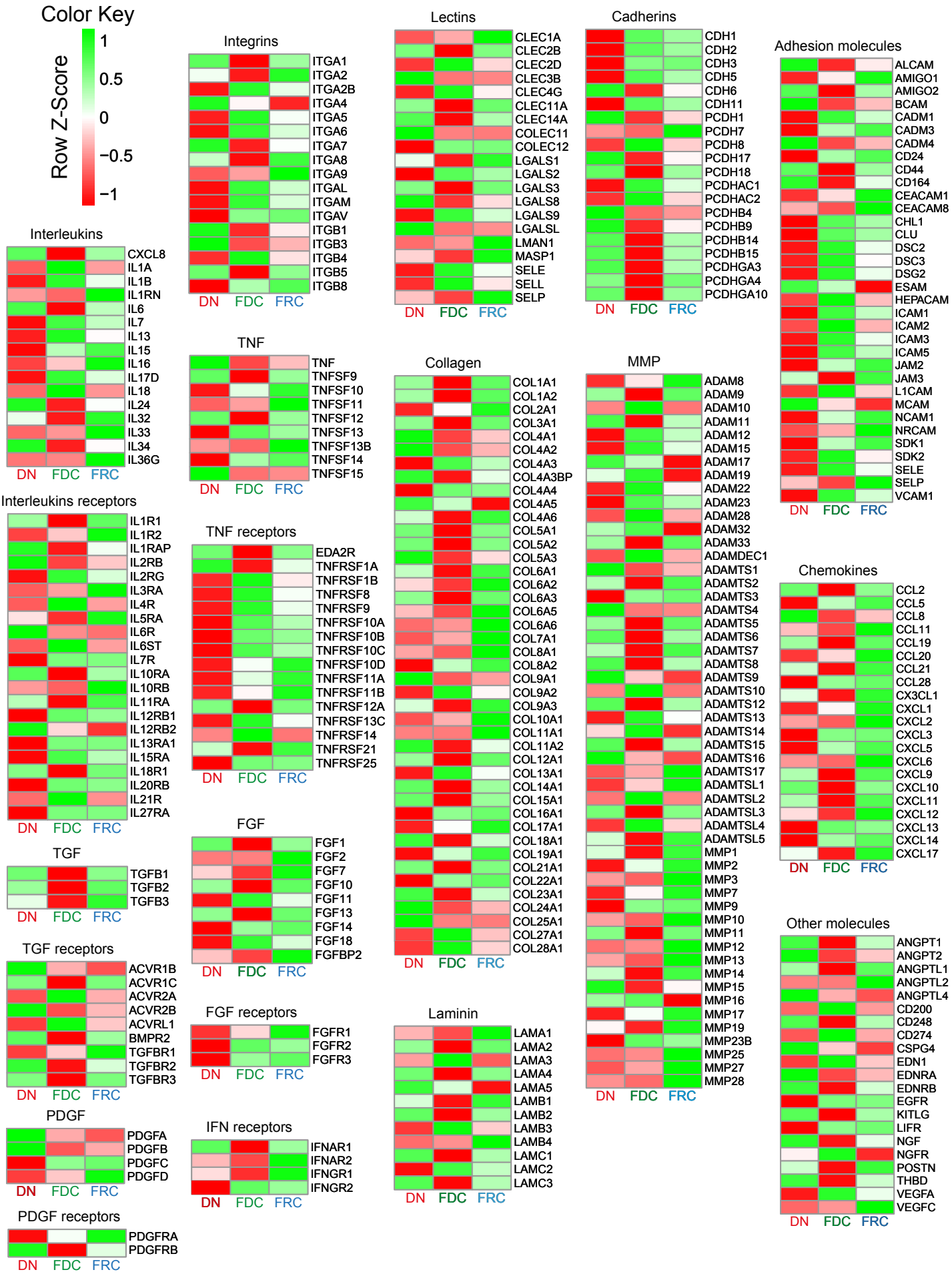

Supplemental Figure 4. Characterization of FRCs (related to Figure 4).

A) Specific gene signatures for FDCs, FRCs, and DNs were compared to signature of mouse LSC subsets previously defined by scRNAseq (Rodda et al., 2016). Seurat score indicating the proximity between human and mouse stromal cell subsets were visualized on violin plots (left panels). Gene signatures of all mouse non-FDC/non-PvC subsets were then merged and Student's t tests were performed to calculate how human FDC, FRC, and DN signatures were significantly enriched in corresponding mouse LSC signatures (right panels).

B) Immunofluorescence on tonsil section for Collagen I (Green) Collagen IV (Red), and Transglutaminase (Blue). Nuclei were counterstained with SytoxBlue (White). Left panels: lower magnification. Scale bar, 100µm. Right panels: higher magnification. Scale bar, 10µm.

C) Expression of stroma markers on LSC subsets after short-term *in vitro* expansion was evaluated by flow cytometry. $CD49a^{-}$ $PDPN^{+}$ LSCs and $CD49a^{+}$ $PDPN^{+}$ LSCs (FRCs) were seeded in culture directly after sorting and analyzed at the end of the first passage before their use for functional experiments. Red histogram shows isotype control and blue histogram the expression of the corresponding marker.

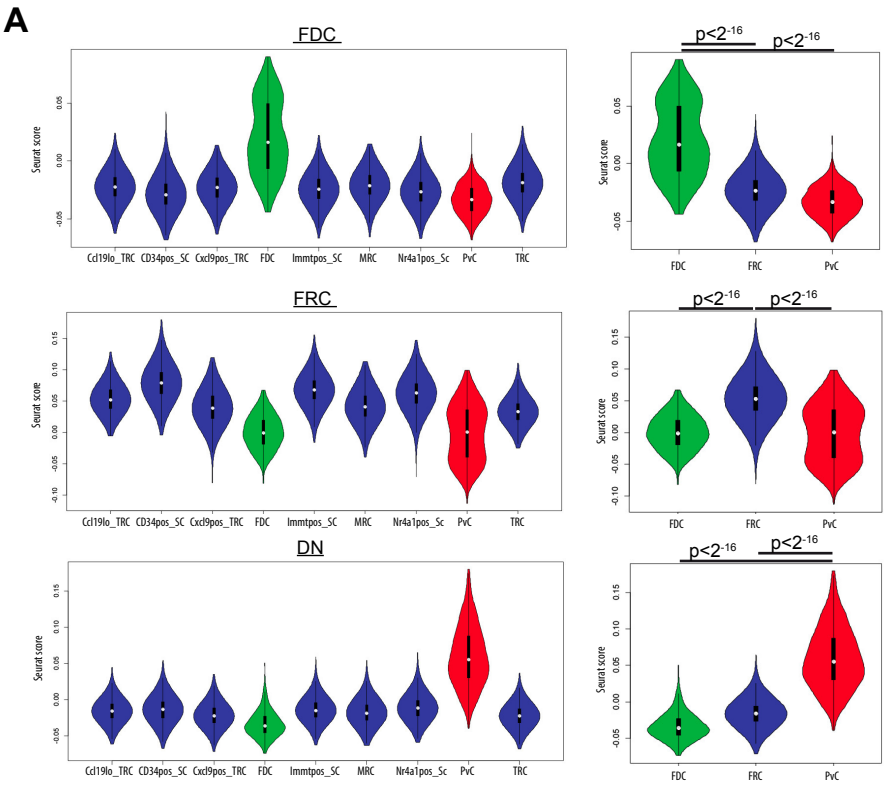

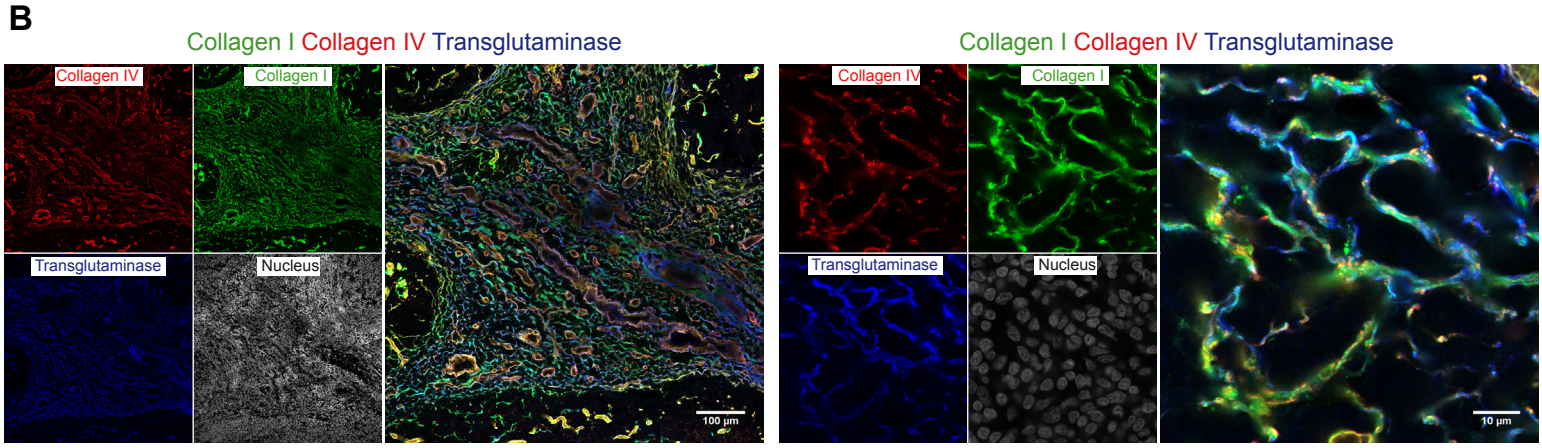

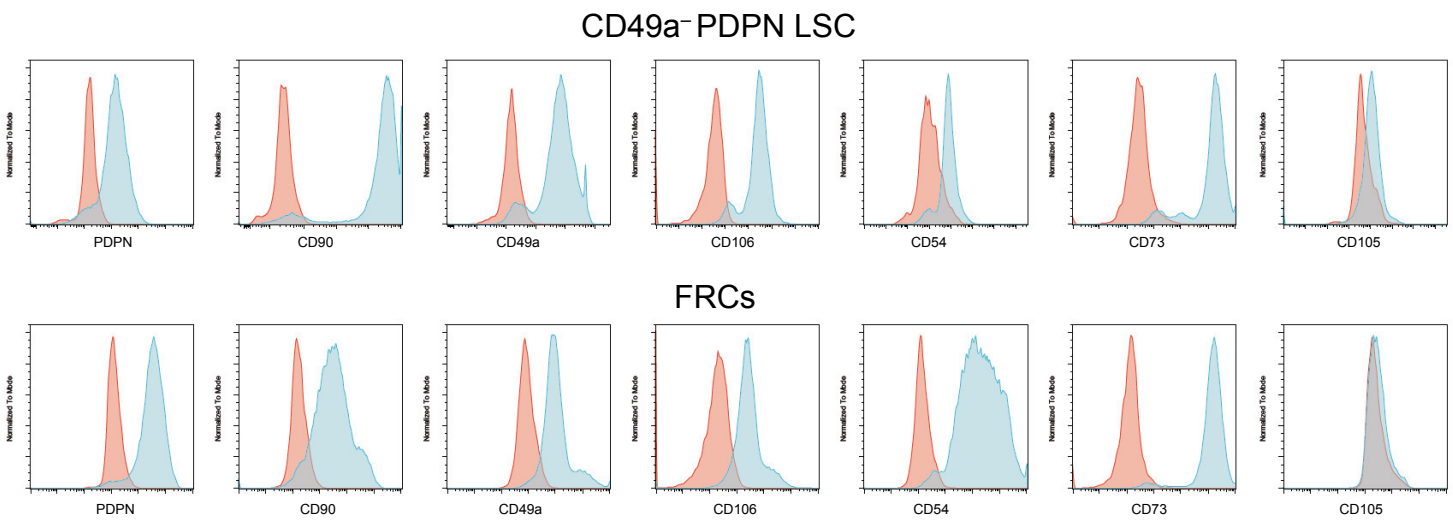

Supplemental Figure 5. FOXP4 is specifically expressed by FDCs (related to Figure 5).

A) Immunofluorescence on section of tonsil GC for TGM2/Transglutaminase (Green) FOXP4 (Red), and CD21 (Blue). Nuclei were counterstained with SytoxBlue (White). Scale bar, 50µm.

B) Immunofluorescence on FDC-enriched cells. After enrichment by Percoll gradient, FDCs were fixed and incubated with a control isotype (green) and CD21 (blue, left), or with FOXP4 and CD21 (right). Nuclei were conterstained with SytoxBlue.

A

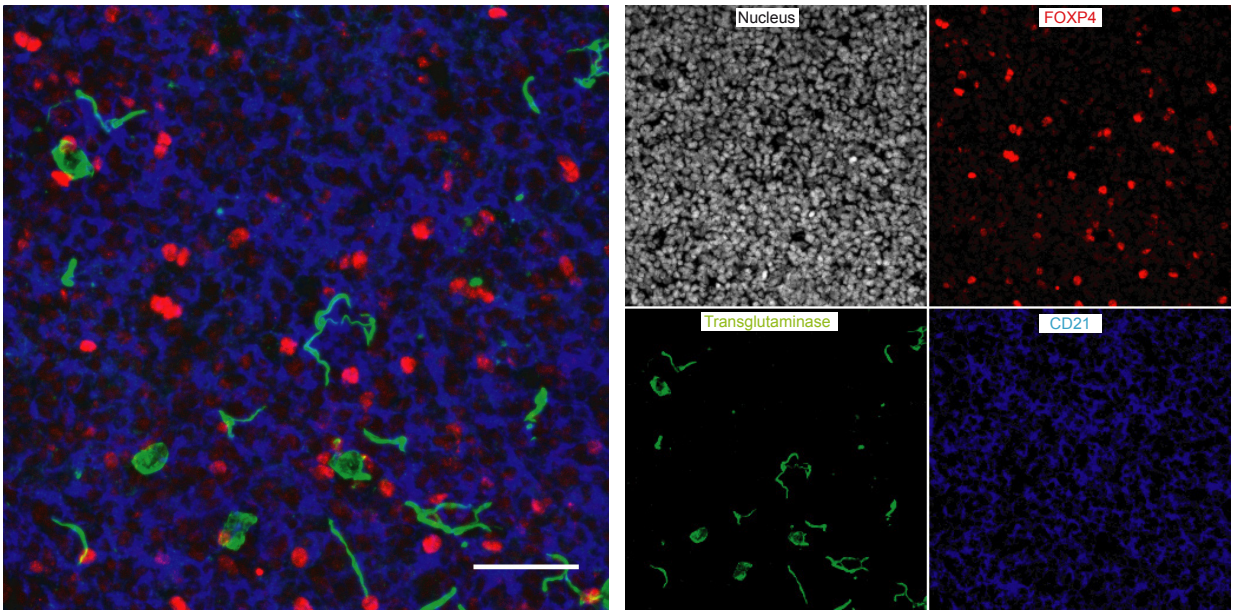

B

FDC-enriched cells

Ctrl CD21 Nucleus

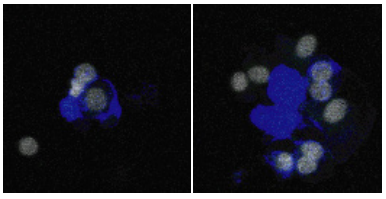

FOXP4 CD21 Nucleus

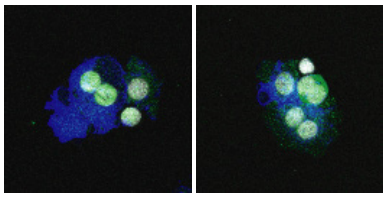

Supplemental Figure 6. Analysis of FL-LSCs (related to Figure 6).

A) Comparative analysis of secondary lymphoid organs by immunohistofluorescence: reactive lymph node, tonsil, and FL lymph node. Sections were stained for CD20 (Green), CD49a (Red), CD21 (Blue), and Transglutaminase (Cyan). Scale bar, 200µm.

B) Chemokine expression was determined in FRCs and FDCs purified from normal *versus* FL samples by RNAseq analysis.

C) Chemokine receptor expression was determined in centrocyte (CC) *versus* d FL B cells by microarrays analysis.

D) GC-confinement receptor expression was determined in CC *versus* FL B cells by microarrays analysis.

E) Expression of receptors and signaling molecules involved in the TGFβ pathway was determined in CC *versus* FL B cells by microarrays analysis.

F) Expression of cytokines was determined in CC *versus* FL B cells by microarrays analysis. Expression of TNF receptors was determined in FRCs and FDCs purified from normal *versus* FL samples by RNAseq analysis.

G) TGFβ receptor expression was determined in FRCs and FDCs purified from normal *versus* FL samples by RNAseq analysis.

H) Expression of mature LSC markers in DN *versus* FL-DNs cells was determined by RNAseq analysis.

***B-H**) * P < .05, ** P < .01, *** P < .001, **** P < .0001*

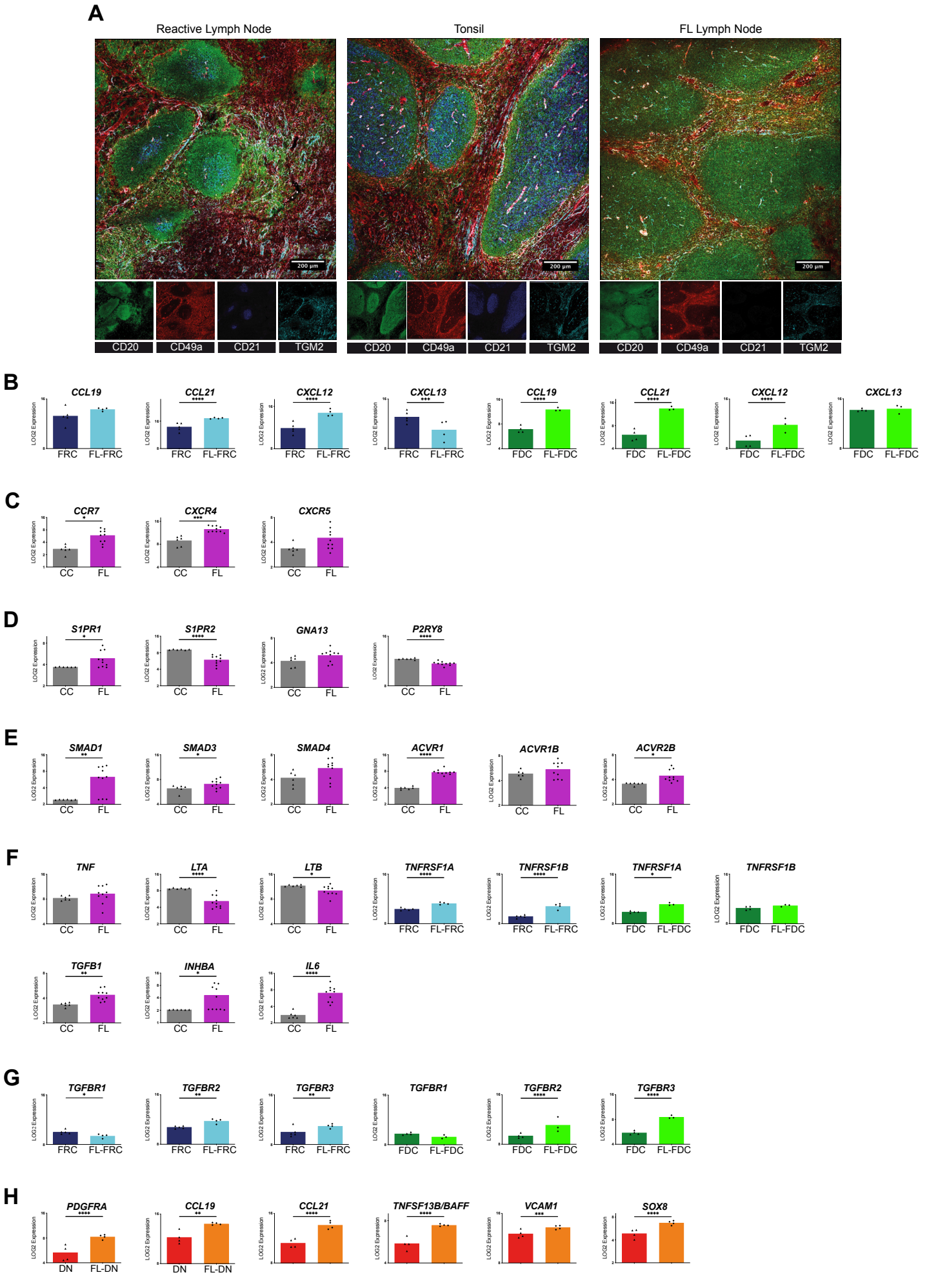
A
Reactive Lymph Node
Tonsil
FL Lymph Node
200 µm
CD20
CD49a
CD21
TGM2
B
CCL19
CCL21
CXCL12
CXCL13
CCL19
CCL21
CXCL12
CXCL13
FRC
FL-FRC
FDC
FL-FDC
C
CCR7
CXCR4
CXCR5
CC
FL
D
S1PR1
S1PR2
GNA13
P2RY8
E
SMAD1
SMAD3
SMAD4
ACVR1
ACVR1B
ACVR2B
F
TNF
LTA
LTB
TNFRSF1A
TNFRSF1B
TNFRSF1A
TNFRSF1B
TGFB1
INHBA
IL6
G
TGFBR1
TGFBR2
TGFBR3
TGFBR1
TGFBR2
TGFBR3
H
PDGFRA
CCL19
CCL21
TNFSF13B/BAFF
VCAM1
SOX8
DN
FL-DN
LOG2 Expression

Supplemental Figure 7. Staining of marginal reticular cells in different secondary lymphoid organs (related to Figure 6).

A) Immunofluorescence on tonsil and FL lymph node (LN) sections for CD20 (Green) TRANCE (Red), and Transglutaminase (Blue), Nuclei were counterstained with SytoxBlue (White). Scale bar, 200μm.

B) Immunofluorescence on a reactive LN section for CD20 (Green) TRANCE (Red), and Transglutaminase (Blue). Nuclei were counterstained with SytoxBlue (White). Left panel: scale bar, 200μm. Right panel: scale bar, 40μm.